J Eng Math (2009) 64:49–80
DOI 10.1007/s10665-008-9247-x

Thin-ship theory and influence of rake and flare

Francis Noblesse · Gerard Delhommeau · Hyun Yul Kim · Chi Yang

Received: 22 April 2008 / Accepted: 1 September 2008 / Published online: 11 October 2008

Abstract The basic computational task of the thin-ship theory of free-surface potential flow about a ship that advances at constant speed along a straight path in calm water, of large depth and lateral extent, is considered. Specifically, a straightforward method for evaluating the pressure and the wave profile at a ship hull (the wave drag, hydrodynamic lift and pitch moment, and sinkage and trim are also considered) in accordance with Michell's thin-ship theory is given. A main ingredient of this method is a simple analytical approximation to the local-flow component in the expression for the Green function (associated with the classical Michell–Kelvin linearized free-surface boundary condition) of thin-ship theory. This practical Green function is used to evaluate and analyze steady flow about a four-parameter family of ship bows with rake and flare. In particular, the variations of the bow-wave height and location with respect to the draft-based Froude number, the entrance angles at the top and bottom waterlines, and the rake angle are explored via a systematic parametric study. This parametric study provides estimates—immediately useful for design—of the influence of rake and flare on the height and the location of a ship bow wave, and shows that rake and flare effects can be significant, especially at low Froude numbers.

Keywords Bow flare · Bow rake · Green function · Ship bow wave · Thin-ship theory

F. Noblesse (✉)
David Taylor Model Basin, NSWCCD, West Bethesda, MD, USA
e-mail: francis.noblesse@navy.mil

G. Delhommeau
Laboratoire de Mécanique des Fluides (UMR CNRS n^{o} 6598), École Centrale, Nantes, France
e-mail: gerard.delhommeau@ec-nantes.fr

H. Y. Kim · C. Yang
Department of Computational and Data Sciences, George Mason University, Fairfax, VA, USA

H. Y. Kim
e-mail: hki4@gmu.edu

C. Yang
e-mail: cyang@gmu.edu

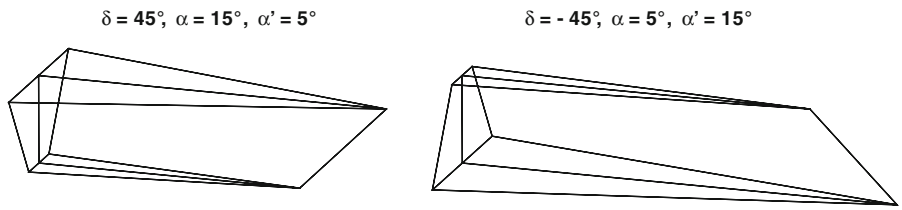

Fig. 1 Two examples of the four-parameter family of ship bows considered in the study

1 Introduction

The bow wave generated by a ship with a wedged-shaped bow that advances at constant speed V_s in calm water (of effectively infinite depth and lateral extent) is considered in [1], where several simple analytical relations are given. In particular, expressions that define the height of the bow wave, the distance between the ship stem and the crest of the wave, the rise of water at the stem, and the bow wave profile are given in [1]. The class of ship bows considered in [1] is defined by two parameters: the draft D of the bow and the waterline entrance angle 2α. Steady flow about this two-parameter family of ship bows likewise depends on two parameters: the waterline entrance angle 2α and the draft-based Froude number $F \equiv V_s/\sqrt{gD}$, where g stands for the acceleration of gravity. The comparisons between the analytical relations and experimental measurements given in [1] show that, in spite of their remarkable simplicity, these analytical relations are sufficiently accurate to be useful for practical design applications, notably at early stages (concept and preliminary design).

However, the practical usefulness of the relations given in [1] is limited by the fact that the two-parameter family of ship bows considered in this study is overly restrictive for many applications. Indeed, typical ship bows, notably bows of fast ships, have significant rake and flare. The effects of rake and flare, ignored in [1], must then be taken into account to design a ship bow, particularly for a fast ship. The wave created by a ship bow with rake and flare is considered here.

Specifically, we consider ship bows that depend on four parameters: the draft D of the ship bow, the entrance angle 2α at the top waterline (at the free surface), the rake angle δ (angle between the ship stem and the vertical) and the hull flare, controlled by $\alpha - \alpha'$ where $2\alpha'$ is the entrance angle at the bottom waterline (at the ship draft). In fact, the hull flare is also affected by the rake angle δ. Two examples of the four-parameter family of ship bows considered here are shown in Fig. 1 for rake angles $\delta = 45°$ (left side) or $\delta = -45°$ (right), top-waterline entrance angles $2\alpha = 30°$ (left) or $10°$ (right) and bottom-waterline entrance angles $2\alpha' = 10°$ (left) or $30°$ (right). The four-parameter family of ship bows depicted in Figs. 1 and 24 is sufficiently general to encompass a large class of fast ships. The flow (notably the bow wave, of particular interest in this study) due to this four-parameter family of ship bows depends on four parameters: $F \equiv V_s/\sqrt{gD}$, δ, α and α'. The two-parameter family of wedge-shaped ship bows considered in [1–3] corresponds to the special case $\delta = 0$ and $\alpha' = \alpha$.

Alternative methods for evaluating steady free-surface flow about ships have been considered in the literature. These methods include semi-analytical theories based on various approximations (thin-ship, slender-ship, 2d + t theories), potential-flow panel (boundary integral equation) methods that rely on the use of a Green function (elementary Rankine source, or Havelock source that satisfies the radiation condition and the Michell linearized free-surface boundary condition), and computational fluid dynamics (CFD) methods that solve the Euler or RANS equations. These alternative calculation methods are reported in a huge body of literature, not reviewed here. A partial list of illustrative references may be found in [1].

In principle, any of the alternative methods reported in the literature can be used to evaluate steady flow about the four-parameter family of ship bows considered here. In practice, however, most of these methods are ill suited for the systematic parametric studies required for our practical goal of obtaining simple analytical relations immediately useful for ship design. In fact, selection of a calculation method suited for systematic parametric studies or for early design (concept and preliminary design) present similar issues, which involve consideration of a tradeoff between competing requirements with respect to accuracy and practicality. Indeed, practical tools that are simple to use and

highly efficient, but need not be highly accurate, are required to quickly evaluate the large number of alternative designs that typically need to be considered for concept design and preliminary design. On the other hand, detail design, and especially design evaluation, involve many fewer choices and require more accurate computational tools, for which efficiency and ease of use are less important considerations.

Thin-ship theory is used here, because this theory is reasonably well suited for the class of fine bows under consideration, and because it significantly simplifies our parametric studies. Specifically, the flow about the four-parameter family of ship bows considered here can be expressed as the product of the factor $(\tan\alpha + \tan\alpha')/2$, which essentially represents an average waterline entrance angle, by a function that depends on three (instead of four) parameters: the (draft-based) Froude number F, the rake angle δ, and a parameter $\varphi \equiv (\tan\alpha - \tan\alpha')/(\tan\alpha + \tan\alpha')$ that is closely related to the hull flare. In fact, this function of F, δ, φ can be expressed in terms of two functions that only depend on the two parameters F and δ.

More generally, Michell's thin-ship theory provides an exceptionally simple and robust method for evaluating steady flow about a ship, and indeed is easily the most successful and most widely used theory of ship wavemaking. This theory has been applied in numerous studies, and in fact is still relevant and useful to this day; notably at early design stages (concept design and preliminary design) and to evaluate flows about fast ships, which typically have fine bows; e.g. [4, 5]. The application of thin-ship theory to steady flow about a ship bow with rake and flare considered here offers an opportunity to revisit the basic computational task of this classical theory, and this opportunity is taken up.

An important property of Michell's thin-ship theory is that variables of main practical interest (wave profile along ship hull, pressure at ship hull, hydrodynamic lift and pitch moment, sinkage and trim, drag) only require flow calculations at the ship centerplane. Thus, Michell's thin-ship theory defines major features of three-dimensional flow about a ship in terms of two-dimensional calculations. In particular, the 2d thin-ship representation of 3d flow about a ship stated in the next section involves a Green function that only depends on two coordinates (instead of three). This Green function of thin-ship theory is reconsidered here, and a remarkably simple analytical expression for the local-flow component in the expression for the 'thin-ship-theory Green function' is given. This highly simplified Green function provides a practical basis for efficiently evaluating the hydrodynamic pressure and wave profile at the hull of a thin ship.

2 Michell's thin-ship approximation

Steady potential flow about a ship, of length L_s, that advances in calm water (of effectively infinite depth and lateral extent) with constant speed V_s along a straight path is considered. The X axis is taken along the path of the ship and points toward the ship bow. The Z axis is vertical and points upward, and the mean free surface is taken as the plane $Z = 0$. The ship hull is symmetric about the vertical plane $Y = 0$. The flow is observed from a moving system of coordinates attached to the ship and thus appears steady. The flow velocity in this system of coordinates is given by $(U - V_s, V, W)$ where (U, V, W) is the flow due to the ship. Nondimensional coordinates and flow velocity are defined in terms of a characteristic reference length L_{ref}, e.g. the ship length L_s or draft D, and the ship speed V_s as

$$\mathbf{x} \equiv (x, y, z) \equiv (X, Y, Z)/L_{\text{ref}}, \quad \mathbf{u} \equiv (u, v, w) \equiv (U, V, W)/V_s. \tag{1}$$

The Froude number F is defined as

$$F = V_s/\sqrt{gL_{\text{ref}}}, \tag{2}$$

where g stands for the acceleration of gravity.

Hereinafter, $\widetilde{\mathbf{x}}$ and $\widetilde{\mathbf{u}}$ stand for a point within the flow region and the corresponding flow velocity. The ship hull surface is defined as

$$y = \pm b(x, z) \quad \text{with } (x, z) \text{ inside } H_0. \tag{3}$$

Here H_0 stands for the portion of the plane $y = 0$ located inside the ship hull, called 'ship centerplane' hereinafter. Within the thin-ship approximation, the flow due to the ship is defined in terms of a distribution of sources, with

strength $-2b_x$ (where $b_x \equiv \partial b/\partial x$) as readily follows from the boundary condition at the ship hull, distributed over the ship centerplane H_0. The flow velocity $\widetilde{\mathbf{u}}$ is then given by

$$\widetilde{\mathbf{u}} = -2 \int\int_{H_0} \mathrm{d}x\mathrm{d}z \widetilde{\nabla} G(x, 0, z\,; \widetilde{\mathbf{x}}) b_x(x, z), \tag{4}$$

where $\widetilde{\nabla} \equiv (\partial/\partial\widetilde{x}, \partial/\partial\widetilde{y}, \partial/\partial\widetilde{z})$ and $G(\mathbf{x}; \widetilde{\mathbf{x}})$ represents the velocity potential of the flow created at a flow-field point $\widetilde{\mathbf{x}}$ by a point source of unit strength located at the source point $\mathbf{x}$. The Green function G satisfies the linear free-surface boundary condition $G_z + F^2 G_{xx} = 0$ at $z = 0$.

The flow is only considered here at flow-field points $(\widetilde{x}, 0, \widetilde{z})$ located at the ship centerplane. Expression (4) then defines the nondimensional hydrodynamic pressure $\widetilde{p}$ at the ship hull as

$$\widetilde{p} \equiv \frac{P}{\rho V_s^2} \approx \widetilde{u} = 2 \int\int_{H_0} \mathrm{d}x\mathrm{d}z \frac{\partial G}{\partial x} b_x. \tag{5}$$

Here, $b_x \equiv b_x(x, z)$ and $G \equiv G(x, z; \widetilde{x}, \widetilde{z}) \equiv G(x, 0, z; \widetilde{x}, 0, \widetilde{z})$. Furthermore, the relation $\partial G/\partial\widetilde{x} = -\partial G/\partial x$ was used in (5). The elevation E of the free surface at a flow field point $(\widetilde{x}, 0, 0)$ is given by

$$\widetilde{e} \equiv Eg/V_s^2 = \widetilde{u}. \tag{6}$$

Thus, the main computational task of thin-ship theory is the evaluation of (5), which defines the hydrodynamic pressure $\widetilde{p}$ and the wave profile $\widetilde{e}$ at the ship hull. This basic and classical task—considered in numerous studies, e.g. [5–10]—is revisited here.

3 Green function of thin-ship theory

The Green function G of thin-ship theory is considered first. We define a, c and d as

$$a \equiv \frac{x - \widetilde{x}}{F^2}, \quad c \equiv \frac{z + \widetilde{z}}{F^2} \le 0, \quad d \equiv \sqrt{a^2 + c^2} \equiv \frac{r_1}{F^2} \equiv \frac{\sqrt{(x - \widetilde{x})^2 + (z + \widetilde{z})^2}}{F^2}, \tag{7}$$

where F is the Froude number (2). The coordinates a and c and the related distance d between the source point $(x, 0, z)$ and the mirror image $(\widetilde{x}, 0, -\widetilde{z})$ of the flow-field point $(\widetilde{x}, 0, \widetilde{z})$ with respect to the mean free-surface plane $z = 0$ are nondimensional with respect to the reference length $L_{\mathrm{ref}} = V_s^2/g$. We also define ρ, θ and ψ as

$$0 \le \rho \equiv \frac{d}{1 + d} \le 1, \quad 0 \le \theta \equiv \frac{-c}{d} \le 1, \quad 0 \le \psi \equiv \frac{-c}{d + |a|} \le 1. \tag{8}$$

We have

$$\psi = \theta/(1 + \sqrt{1 - \theta^2}), \quad \theta = 2\psi/(1 + \psi^2). \tag{9}$$

Expressions (7) in [11] or (13)–(16) in [12] yield

$$G = G^S + G^L + G^W, \tag{10}$$

where G^S, G^L and G^W represent the fundamental free-space singularity, a local-flow component, and waves, respectively. The free-space singularity G^S is given by

$$4\pi G^S = -1/r \quad \text{with } r = \sqrt{(x - \widetilde{x})^2 + (z - \widetilde{z})^2}. \tag{11}$$

The wave component G^W is given by

$$4\pi G^W = H(x - \widetilde{x})\, \frac{8}{F^2}\, \mathfrak{Im} \int_0^\infty \mathrm{d}t\, \mathrm{e}^{(1+t^2)(z+\widetilde{z})/F^2 - \mathrm{i}\sqrt{1+t^2}(x-\widetilde{x})/F^2}, \tag{12}$$

where $H(\cdot)$ is the Heaviside unit-step function and $\mathfrak{Im}$ means imaginary part.

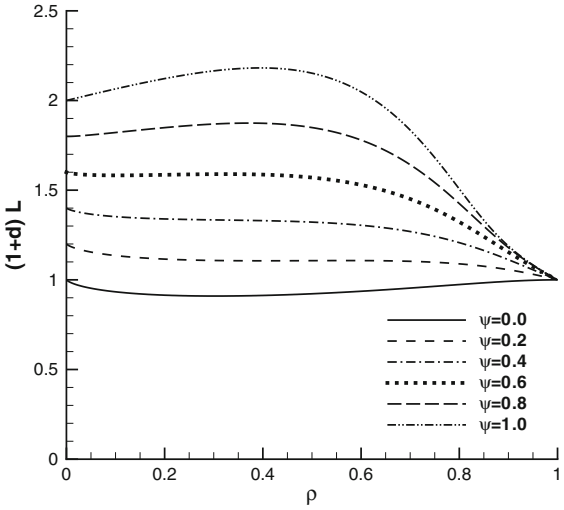

Fig. 2 Function $(1+d)L$

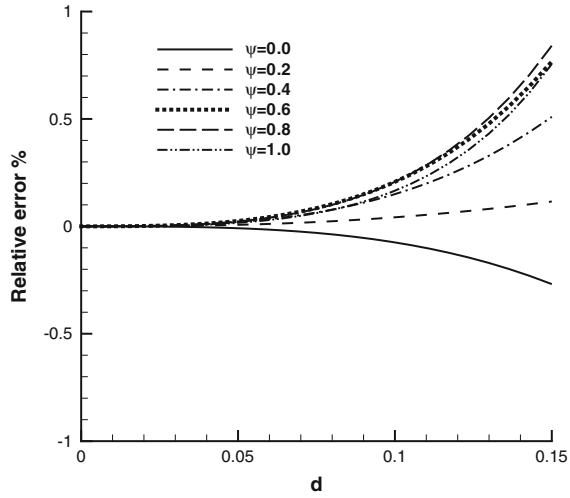

Fig. 3 Relative error associated with the three-term nearfield approximation (15)

Expressions (1) and (3) in [13] or (13)–(15) and (18a) in [12] show that the local-flow component G^L can be expressed as

$$4\pi F^2 G^L \equiv g^L = 1/d - 2L, \tag{13}$$

where d is given by (7) and L is defined as

$$L = 1 + \psi - \frac{2}{\pi}\int_0^1 \mathrm{d}t\ \Im\mathfrak{m}\ [\mathrm{e}^A E_1(A) + \log(A) + \gamma]. \tag{14a}$$

Here, ψ is given by (8), $\gamma = 0.577\ldots$ is Euler's constant, $E_1(\cdot)$ is the usual exponential integral, and A is defined as

$$A \equiv c(1-t^2) + \mathrm{i}\,|a|\sqrt{1-t^2} \tag{14b}$$

with c and a given by (7). The integral in (14a) is null if $A = 0$, i.e., if $d = 0$. We then have $1 \le L \sim 1 + \psi \le 2$ as $d \to 0$. Thus, the function L is finite as $d \to 0$. Figure 2 depicts the function $(1+d)L$ for $0 \le \rho \le 1$ with $\psi = 0, 0.2, \ldots, 1$.

4 Nearfield and farfield approximations to local-flow component

Expression (5) in [13], with (8) and (9) of the present study, yield the nearfield approximation

$$g^L \sim \frac{1}{d} - 2(1+\psi) - d\,\frac{1+\psi}{1+\psi^2}\left[(1-\psi)\left(\log\frac{d/2}{1+\psi^2} + \gamma - \frac{1}{2} + \frac{\psi^2}{6}\right) - \frac{8}{3}\,\psi\right] \quad \text{as } d \to 0. \tag{15}$$

The relative error associated with the three-term nearfield approximation (15) is depicted in Fig. 3 for $0 \le d \le 0.15$. This figure shows that the nearfield approximation (15) yields a relative error smaller than 1% for $d \le 0.15$.

The integral representation (14) is well suited for numerical evaluation for small and moderate values of d, i.e., in the nearfield. For large values of d, i.e., in the farfield, [14] yields the nine-term farfield asymptotic approximation

$$g^L \sim \frac{-1}{d} - 2\frac{\theta - 1/(1+\theta)}{d^2} - \frac{6\,\theta}{d^3}\left(\theta - \frac{2+\theta}{(1+\theta)^2}\right) - \frac{6}{d^4}\left(5\,\theta^3 + \frac{\Delta_3}{(1+\theta)^3}\right)$$
$$- \frac{30\,\theta}{d^5}\left(7\,\theta^3 + \frac{\Delta_4}{(1+\theta)^4}\right) - \frac{90}{d^6}\left(21\,\theta^5 - \frac{\Delta_5}{(1+\theta)^5}\right) - \frac{1890\,\theta}{d^7}\left(11\,\theta^5 - \frac{\Delta_6}{(1+\theta)^6}\right)$$
$$- \frac{630}{d^8}\left(429\,\theta^7 + \frac{\Delta_7}{(1+\theta)^7}\right) - \frac{5670\,\theta}{d^9}\left(715\,\theta^7 + \frac{\Delta_8}{(1+\theta)^8}\right) \text{ as } d \to \infty \tag{16}$$

with

$$\begin{aligned}
\Delta_3 &= 1 + 3\,\theta - 15\,\theta^2 - 18\,\theta^3 - 6\,\theta^4,\\
\Delta_4 &= 4 + 16\,\theta - 20\,\theta^2 - 55\,\theta^3 - 40\,\theta^4 - 10\,\theta^5,\\
\Delta_5 &= 1 + 5\,\theta - 15\,\theta^2 - 115\,\theta^3 - 15\,\theta^4 + 250\,\theta^5 + 330\,\theta^6 + 175\,\theta^7 + 35\,\theta^8,\\
\Delta_6 &= 2 + 12\theta + 6\,\theta^2 - 104\,\theta^3 - 118\,\theta^4 + 111\,\theta^5 + 336\,\theta^6 + 301\,\theta^7 + 126\,\theta^8 + 21\,\theta^9,\\
\Delta_7 &= 5 + 35\,\theta - 91\,\theta^2 - 1197\,\theta^3 - 2331\,\theta^4 + 4515\,\theta^5 + 12229\,\theta^6 + 3430\,\theta^7\\
&\quad - 17654\,\theta^8 - 27342\,\theta^9 - 18690\,\theta^{10} - 6468\,\theta^{11} - 924\,\theta^{12},\\
\Delta_8 &= 40 + 320\,\theta + 440\,\theta^2 - 3200\,\theta^3 - 11768\,\theta^4 - 64\,\theta^5 + 34200\,\theta^6 + 38709\,\theta^7\\
&\quad - 16752\,\theta^8 - 78324\,\theta^9 - 83952\,\theta^{10} - 46530\,\theta^{11} - 13728\,\theta^{12} - 1716\,\theta^{13}.
\end{aligned} \tag{17}$$

The approximation (16), where $1 \le n \le 9$ terms are used, provides a hierarchy of farfield approximations. The first two terms in the farfield approximation (16) agree with (13) and (20a) in [12] and with (12)–(15) in [15]. The relative errors associated with the farfield asymptotic approximations (16) with $2 \le n \le 9$ are depicted in Fig. 4 for $0.85 \le \rho \le 1$ with $\theta = 0, 0.2, \ldots, 1$. These figures show that six terms in the asymptotic approximation (16) are optimal to obtain a 1% relative error. Specifically, the six-term approximation (16) yields a relative error smaller than 1% for $6 \le d$, which corresponds to ρ larger than approximately 0.86.

Thus, the 3-term nearfield approximation (15) and the 6-term farfield approximation (16)–(17) yield relative errors smaller than 1% for $d \le 0.15$ and $6 \le d$, respectively. A midfield approximation that yields comparable accuracy for $0.15 < d < 6$ is given further on.

The nearfield approximation (15) and the farfield approximation (16) show that the local-flow component g^L behaves approximately like a unit sink in the near field and a unit source in the farfield. Indeed, g^L can be expressed as

$$g^L = Q/d \quad \text{with } Q \equiv 1 - 2dL. \tag{18}$$

We have $Q \to 1$ as $d \to 0$ and $Q \to -1$ as $d \to \infty$. This property is illustrated in Fig. 5, which depicts the 'equivalent source strength' Q for $0 \le \rho \le 1$ with $\psi = 0, 0.2, \ldots, 1$.

5 Simple approximation to local-flow component

A rough approximation to the function $(1+d)L$ depicted in Fig. 2 is $1 + \psi(1-\rho) \equiv 1 + \psi/(1+d)$. A rough approximation to the function

$$(1+d)L - 1 - \psi/(1+d), \tag{19a}$$

depicted in Fig. 6 for $0 \le \rho \le 1$ with $\psi = 0, 0.2, \ldots, 1$, is

$$2.3\psi^2\rho(1-\rho) \equiv 2.3\,\psi^2 d/(1+d)^2. \tag{19b}$$

Expressions (13) and (19) yield the approximation $g^L \approx g_a^L$ with

$$g_a^L \equiv \frac{1}{d} - \frac{2}{1+d} - \frac{2\psi}{(1+d)^2}\left(1 + \frac{2.3\,\psi\,d}{1+d}\right). \tag{20}$$

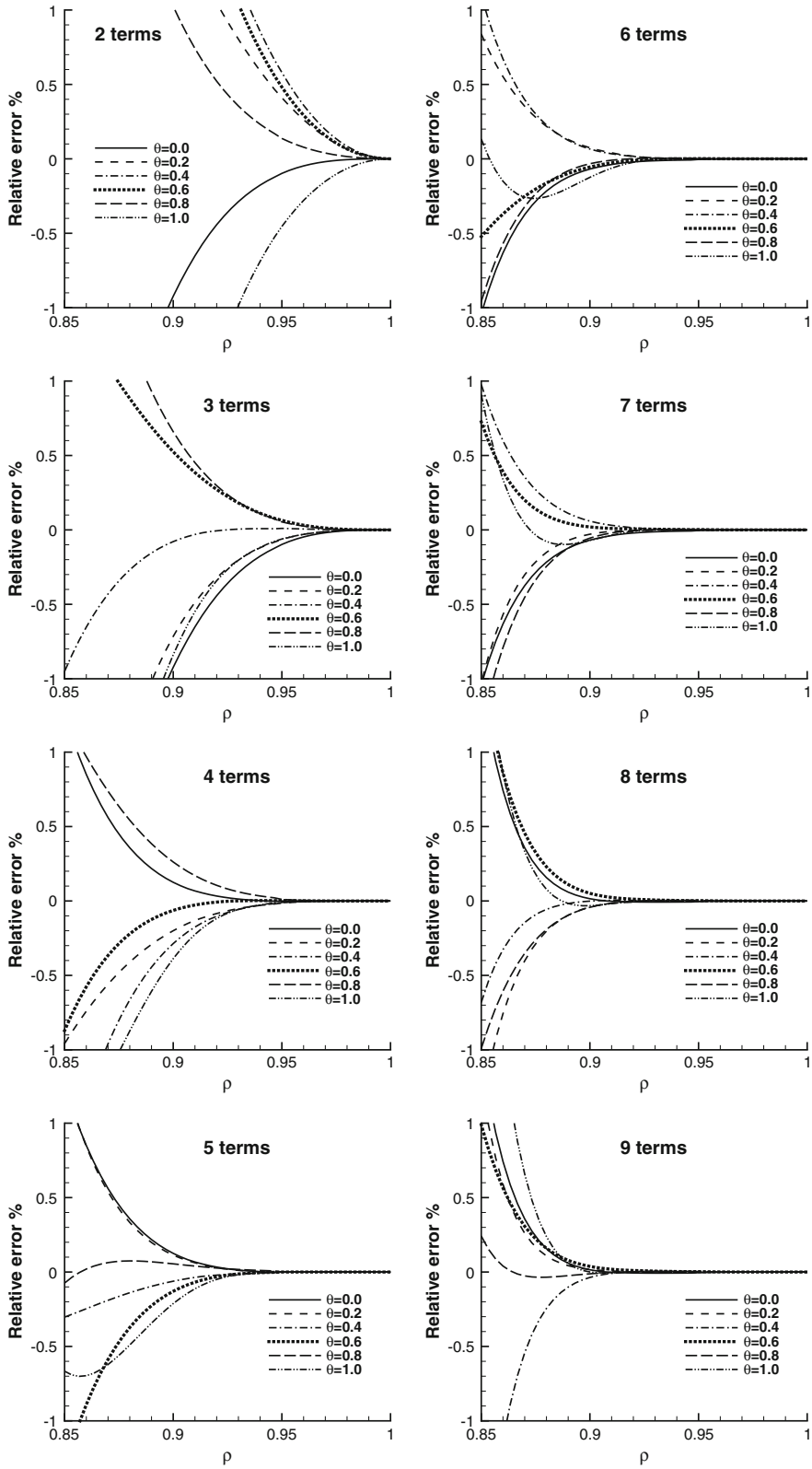

Fig. 4 Relative errors associated with the n-term ($2 \leq n \leq 9$) farfield approximation (16)

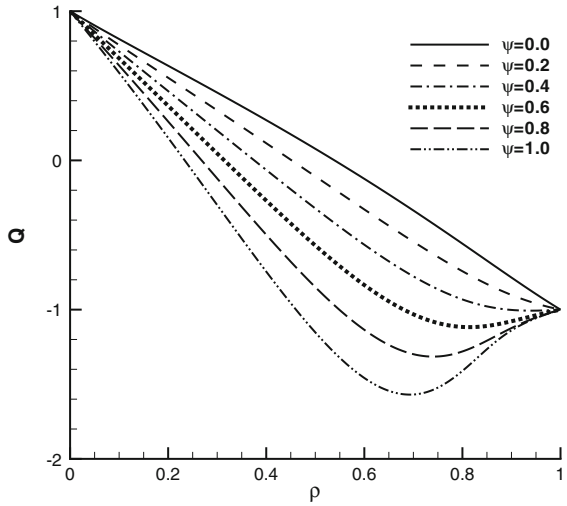

Fig. 5 'Equivalent source strength' Q

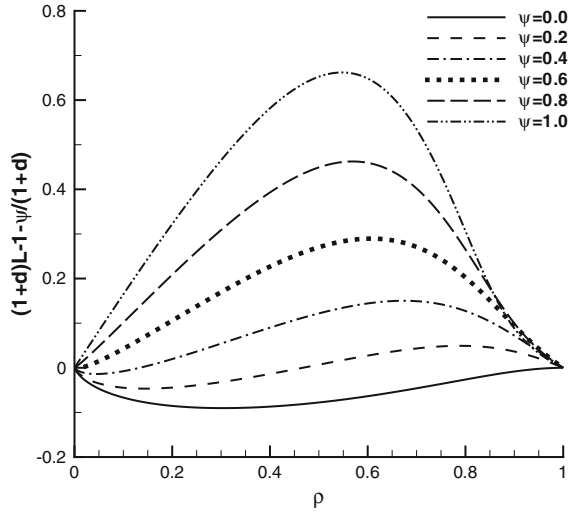

Fig. 6 Function $(1+d)L-1-\psi/(1+d)$

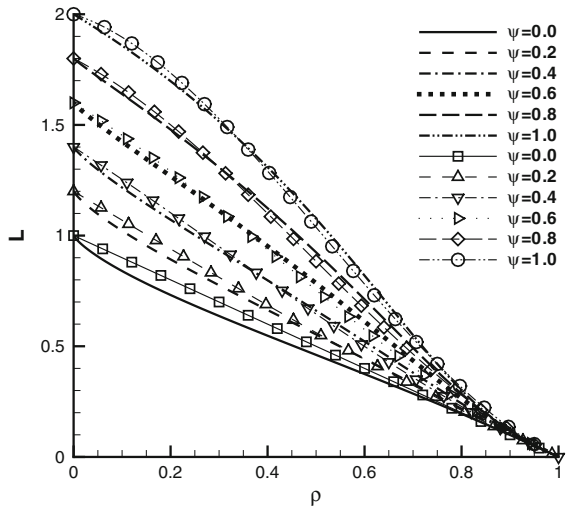

Fig. 7 Function L defined by (14) and function $L_a \equiv (1/d - g_a^L)/2$ associated with the simple analytical approximation (20)

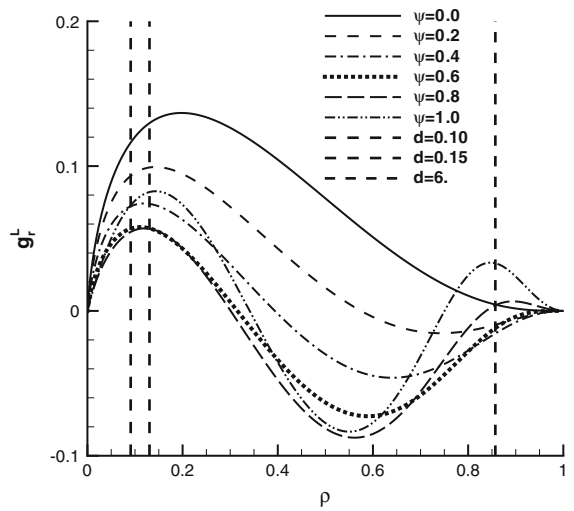

Fig. 8 Function $g_r^L \equiv g^L - g_a^L$

This approximation yields $g_a^L \sim 1/d - 2(1+\psi)$ as $d \to 0$ in agreement with the first two terms in the nearfield approximation (15), and $g_a^L \sim -1/d + 2(1-\psi)/d^2$ as $d \to \infty$ in agreement with the first term (or the first two terms if $\psi = 0$, i.e., along the axis $c = 0$) in the farfield approximation (16). The function L defined by (14) and the function $L_a \equiv (1/d - g_a^L)/2$ associated with the approximation (20) are depicted in Fig. 7 for $0 \le \rho \le 1$ with $\psi = 0, 0.2, \ldots, 1$.

6 Midfield approximation to local-flow component

The local-flow component g^L defined by (13) and (14) is now expressed as

$$g^L = g_a^L + g_r^L, \tag{21a}$$

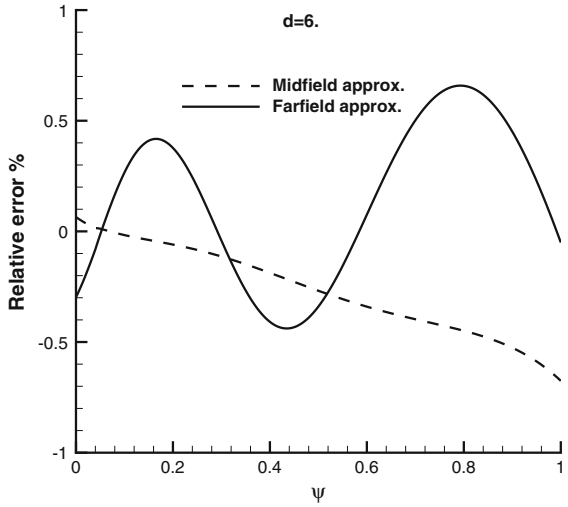

Fig. 9 Relative errors associated with the 6-term farfield approximation (16)–(17) and the midfield approximation (20)–(21) for $d = 6$

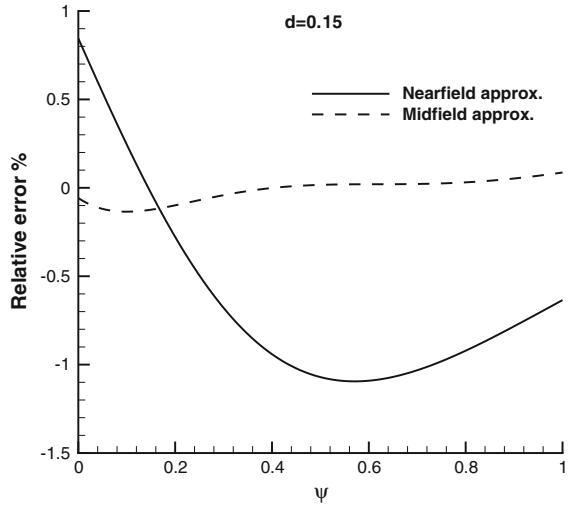

Fig. 10 Relative errors associated with the nearfield approximation (15) and the midfield approximation (20)–(21) for $d = 0.15$

where g_a^L is the approximation (20) and $g_r^L \equiv g^L - g_a^L$ is the corresponding remainder. The function $g_r^L(\rho;\psi)$ is depicted in Fig. 8. The vertical lines $\rho \approx 0.13$ and $\rho \approx 0.86$, which correspond to $d = 0.15$ and $d = 6$, are also shown in Fig. 8. Within the midfield region $0.15 < d < 6$, the remainder g_r^L in (21a) can be evaluated using the polynomial approximation

$$g_r^L \approx 0.0810 - 0.0116\,\psi - 0.1618\,\psi^2 - 0.0076\,\psi^3 + [0.6272 - 0.9676\,\psi + 0.7362\psi^2 + 2.2920\,\psi^3]\rho$$
$$-[2.1560 + 0.7414\,\psi - 0.8938\,\psi^2 + 10.362\psi^3]\rho^2 + [2.1092 + 3.8784\,\psi - 3.4960\,\psi^2 + 16.132\psi^3]\rho^3$$
$$-[0.6644 + 2.1148\,\psi - 2.1338\,\psi^2 + 8.2684\,\psi^3]\rho^4. \tag{21b}$$

The relative errors associated with the 6-term farfield approximation (16)–(17) and the midfield approximation (20)–(21) are depicted in Fig. 9 for $d = 6$ and $0 \le \psi \le 1$. These errors are comparable, and approximately within the range $\pm 0.7\%$. Figure 10 similarly depicts the relative errors associated with the 3-term nearfield approximation (15) and the midfield approximation (20)–(21) for $d = 0.15$ and $0 \le \psi \le 1$. This figure shows that the midfield approximation is more accurate than the nearfield approximation for $d = 0.15$. Indeed, Fig. 11 shows that the nearfield approximation (15) and the midfield approximation (20)–(21) yield comparable errors, approximately within the range $\pm 0.5\%$, for $d = 0.1$. Thus, the 3-term nearfield approximation (15), the 6-term farfield approximation (16)–(17) and the midfield approximation (20)–(21) can be used within the complementary regions $d \le 0.1$, $6 \le d$ and $0.1 < d < 6$, respectively. The vertical lines $d = 0.1$ and $d = 6$ are shown in Fig. 8. The functions L defined by these three complementary approximations and by (14) cannot be distinguished in Fig. 12.

7 Practical Green function

The Green function of thin-ship theory defined by (10)–(14) can finally be expressed as

$$G \equiv G^W + G_a^{SL} + G_r^L. \tag{22}$$

The wave component G^W is defined by the Fourier integral (12). G^W is examined in [16], where a farfield approximation and two complementary nearfield integral representations are given. However, the Fourier–Kochin approach is a more practical approach for evaluating the contribution of the wave component G^W to the hull pressure defined by

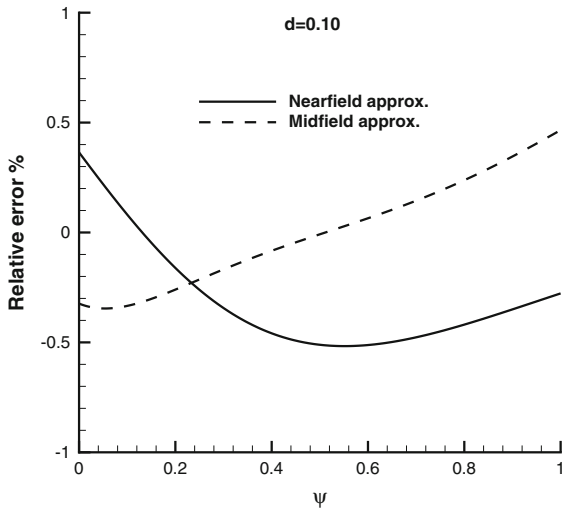

Fig. 11 Relative errors associated with the nearfield approximation (15) and the midfield approximation (20)–(21) for $d = 0.1$

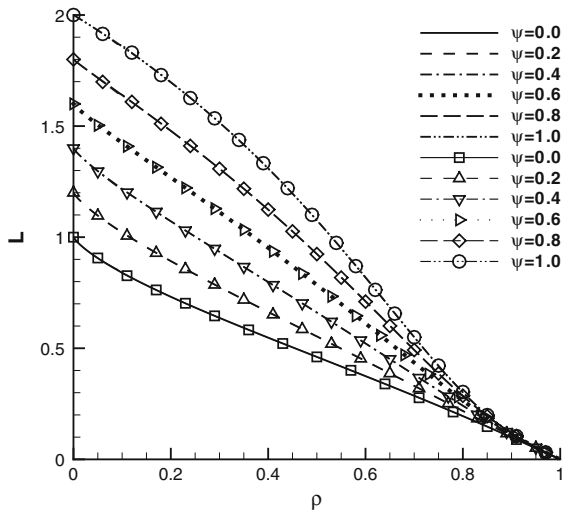

Fig. 12 Function L defined by the integral representation (14) and by the nearfield approximation (15) for $d \leq 0.1$, the farfield approximation (16)–(17) for $6 \leq d$, and the midfield approximation (20)–(21) for $0.1 < d < 6$

(5), and this approach is adopted here. The local-flow component G_a^{SL} in (22) is defined as $4\pi G_a^{SL} \equiv -1/r + g_a^L/F^2$ where g_a^L is the simple approximation (20). Expressions (7) then yield

$$4\pi G_a^{SL} \equiv \frac{-1}{r} + \frac{1}{r_1} - \frac{2}{F^2 + r_1} - \frac{2F^2\psi}{(F^2 + r_1)^2}\left(1 + \frac{2.3\,\psi\, r_1}{F^2 + r_1}\right) \equiv \frac{-1}{r} + 4\pi G_a^L, \tag{23a}$$

where r, r_1 and ψ are defined by (11), (7) and (8) as

$$r = \sqrt{(x - \widetilde{x})^2 + (z - \widetilde{z})^2}, \quad r_1 = \sqrt{(x - \widetilde{x})^2 + (z + \widetilde{z})^2}, \quad \psi = \frac{-(z + \widetilde{z})}{r_1 + |\,x - \widetilde{x}|}. \tag{23b}$$

The remainder G_r^L in (22) is the local-flow component

$$4\pi F^2 G_r^L \equiv g_r^L \equiv g^L - g_a^L \tag{24}$$

which is depicted in Fig. 8. The remainder g_r^L can be evaluated using (24), (20), the nearfield approximation (15), the farfield approximation (16)–(17), and the midfield approximation (21b).

The function g^L defined by the integral representation (13)–(14) and the function g_a^L given by the simple approximation (20) are depicted in Fig. 13 for $0 \leq \rho \leq 1$ with $\psi = 0, 0.2, \ldots, 1$. This figure shows that the simple analytical expression (20) provides a reasonable approximation to the function g^L overall. More precisely, the approximation g_a^L is accurate in both the nearfield, where g^L is singular (specifically, $g^L \sim 1/d$ as $d \to 0$) and the farfield where g^L vanishes ($g^L \sim -1/d$ as $d \to \infty$). Figure 13 shows that the approximation g_a^L is reasonable, although not highly accurate, in the midfield. The highly-simplified Green function,

$$G \approx G_a \equiv G^W + G_a^{SL}, \tag{25}$$

may then be expected to be useful for practical applications. In fact, this conjecture is verified in the next section. The approximate Green function defined by (25), (23) and (12) is less accurate—but considerably simpler—than (22) and the alternative approximations, based on table interpolations [12, 17] or Chebyshev polynomials [18], given in the literature. In particular, the approximation (23) can be used in the entire domain $0 \leq r_1 \leq \infty$. Thus, no division of this domain into subdomains—required for the alternative approximations given in the literature—is needed in (23).

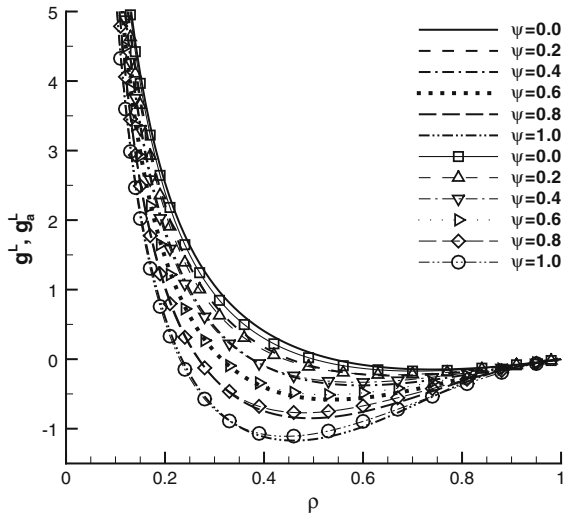

Fig. 13 Functions g^L and g_a^L given by the integral representation (13) and (14) and by the simple analytical approximation (20), respectively

8 Application to wedge-shaped ship bows without rake or flare

The contributions of the wave component G^W, the main local-flow component G_a^{SL} and the remainder G_r^L in (22) to the pressure $\widetilde{p}$ and the free-surface elevation $\widetilde{e}$ defined by (5) and (6) are now considered for a wall-sided wedge-shaped bow (no rake or flare) with draft D and waterline entrance angle 2α. The draft D of the bow is used as reference length L_{ref} in (1) and (2). Thus, the hull centerplane H_0 consists of the rectangular region $-1 \le z \le 0$, $-\ell \le x \le 0$. Here, $\ell \equiv L_b/D$ is the nondimensional length of the ship bow considered here. A bow length $\ell = 4$ is considered for four Froude numbers $F = 0.5$, 1, 2 and 4. These draft-based Froude numbers F correspond to length-based Froude numbers equal to 0.125, 0.25, 0.5 and 1 for a ship with length L_s equal to four times the bow length L_b, and bow length L_b equal to four times the draft D (length/draft ratio $L_s/D = 16$). We have $b_x = -\tan\alpha$ in (5). This expression then defines the hydrodynamic pressure $\widetilde{p}$ and free-surface elevation $\widetilde{e}$ as

$$\begin{aligned} \widetilde{p} &\equiv \widetilde{p}_*(\tan\alpha)/(2\pi) \quad \text{with} \quad \widetilde{p}_* \equiv \widetilde{p}^W + \widetilde{p}_a^{SL} + \widetilde{p}_r^L \equiv \widetilde{p}_a + \widetilde{p}_r^L, \\ \widetilde{e} &\equiv \widetilde{e}_*(\tan\alpha)/(2\pi) \quad \text{with} \quad \widetilde{e}_* \equiv \widetilde{e}^W + \widetilde{e}_a^{SL} + \widetilde{e}_r^L \equiv \widetilde{e}_a + \widetilde{e}_r^L, \end{aligned} \tag{26}$$

where the components $(\cdot)^W$, $(\cdot)_a^{SL}$, $(\cdot)_r^L$, $(\cdot)_a$ correspond to the components G^W, G_a^{SL}, G_r^L, G_a in (22) and (25).

Expressions (5) and (12) yield $\widetilde{p}^W = 0$ for $0 \le \widetilde{x}$, and

$$\widetilde{p}^W = -8 \int_0^\infty \mathrm{d}t \, \frac{1 - \mathrm{e}^{-(1+t^2)/F^2}}{1+t^2} \mathrm{e}^{(1+t^2)\widetilde{z}/F^2} [\sin(\sqrt{1+t^2}\widetilde{x}/F^2) - \widetilde{S}_\ell] \tag{27a}$$

with $\widetilde{S}_\ell \equiv 0$ for $-\ell \le \widetilde{x} \le 0$ and $\widetilde{S}_\ell \equiv \sin[\sqrt{1+t^2}(\widetilde{x}+\ell)/F^2]$ for $\widetilde{x} \le -\ell$. Expressions (5), (23) and (24) yield

$$\widetilde{p}_a^{SL} = \int_{-1}^0 \mathrm{d}z \left[\frac{1}{r} - \frac{1}{r_1} + \frac{2}{F^2 + r_1} + \frac{2F^2\psi}{(F^2+r_1)^2} \left(1 + \frac{2.3\,\psi\, r_1}{F^2 + r_1} \right) \right]_{x=-\ell}^{x=0}, \tag{27b}$$

$$\widetilde{p}_r^L = \frac{-1}{F^2} \int_{-1}^0 \mathrm{d}z \left[g_r^L \right]_{x=-\ell}^{x=0}, \tag{27c}$$

where $[f(x,z;\widetilde{x},\widetilde{z})]_{x=-\ell}^{x=0} \equiv f(x=0,z;\widetilde{x},\widetilde{z}) - f(x=-\ell,z;\widetilde{x},\widetilde{z})$. The components $\widetilde{e}^W$, $\widetilde{e}_a^{SL}$ and $\widetilde{e}_r^L$ to the free-surface elevation $\widetilde{e}_*$ in (26) are given by (27) with $\widetilde{z} = 0$, which yields $1/r - 1/r_1 = 0$ in (27b).

Figure 14 shows the pressures $\widetilde{p}^W + \widetilde{p}_a^{SL} + \widetilde{p}_r^L$ and $\widetilde{p}^W + \widetilde{p}_a^{SL}$ for $-8 \le \widetilde{x} \le 2$ at the top waterline $\widetilde{z} = 0$ (for which $\widetilde{p}$ is identical to the free-surface elevation $\widetilde{e}$) and the bottom waterline $\widetilde{z} = -1$. The wedge-shaped bow

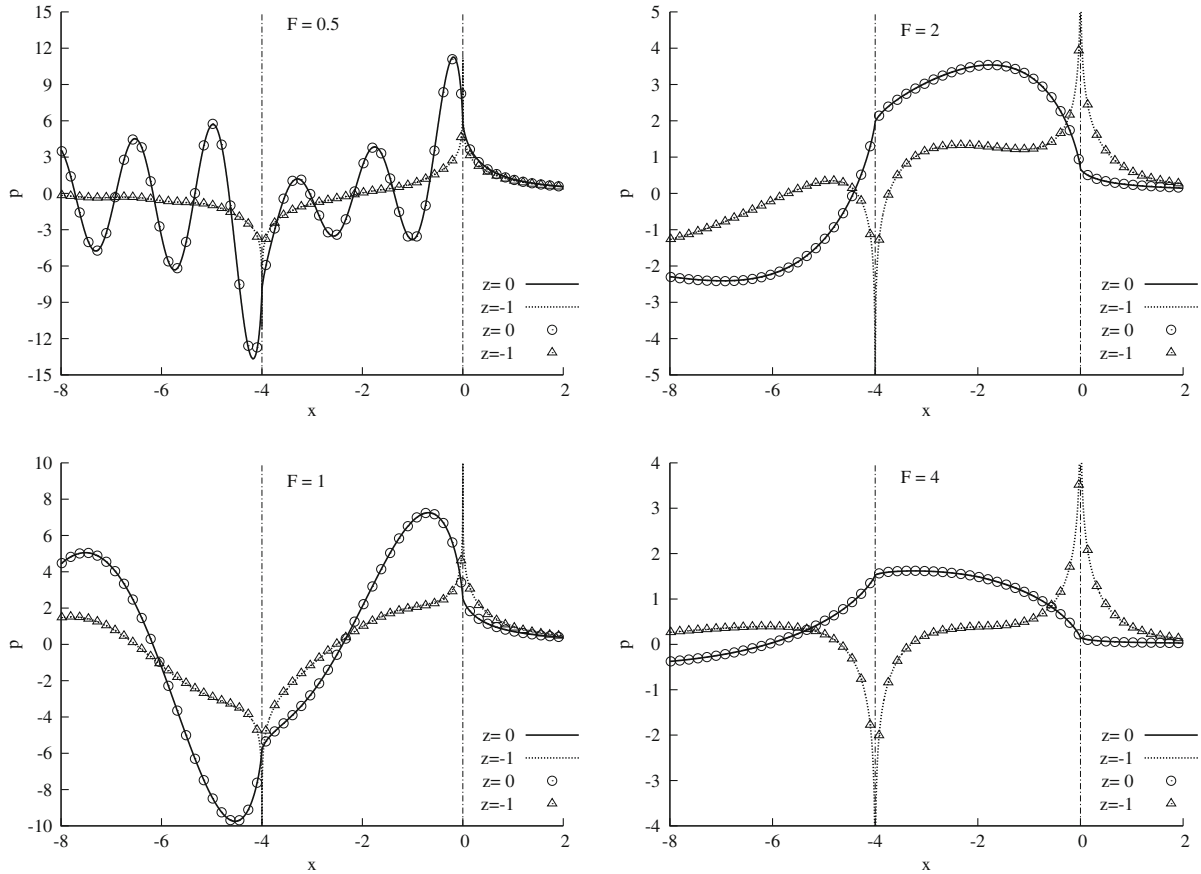

Fig. 14 Pressures $\widetilde{p}^W + \widetilde{p}_a^{SL} + \widetilde{p}_r^L$ (lines) and $\widetilde{p}^W + \widetilde{p}_a^{SL}$ (circles or triangles) for $-8 \le \widetilde{x} \le 2$ at the top waterline $\widetilde{z} = 0$ (for which $\widetilde{p}$ is identical to the free-surface elevation $\widetilde{e}$) and the bottom waterline $\widetilde{z} = -1$ for a wedge-shaped bow between the vertical lines $x = 0$ and $x = -4$

considered here is located between the vertical lines $x = 0$ and $x = -4$ shown in Fig. 14. Four draft-based Froude numbers are considered: $F = 0.5$ (top left corner), $F = 1$ (bottom left), $F = 2$ (top right) and $F = 4$ (bottom right). The pressure $\widetilde{p}^W + \widetilde{p}_a^{SL} + \widetilde{p}_r^L$ and the related approximation $\widetilde{p}^W + \widetilde{p}_a^{SL}$, respectively identified by lines or symbols (circles or triangles) in Fig. 14, cannot be distinguished. This result, which will be further verified in Fig. 15, indicates that the remainder G_r^L in (22) can be neglected, and that the highly simplified approximate Green function $G_a \equiv G^W + G_a^{SL}$ defined by (25) can be used in practice. The simple Green function G_a given by (25), (23) and (12) is then used henceforth.

9 Steady flow about a generic thin ship

The basic computational task of evaluating the hull pressure $\widetilde{p}$ defined by (5), with the simple Green function $G \approx G_a$ given by (25), (23) and (12), is now considered for a generic thin ship defined by (3). The hull pressure $\widetilde{p}$ and the free-surface elevation $\widetilde{e}$ defined by (5) and (6) can be expressed as

$$\widetilde{p} \approx \widetilde{p}_a \equiv \widetilde{p}^W + \widetilde{p}_a^{SL}, \quad \widetilde{e} \approx \widetilde{e}_a \equiv \widetilde{e}^W + \widetilde{e}_a^{SL}, \tag{28}$$

where $(\cdot)_a$ and the components $(\cdot)^W$ and $(\cdot)_a^{SL}$ correspond to the practical Green function G_a given by (25) and the related components G^W and G_a^{SL}.

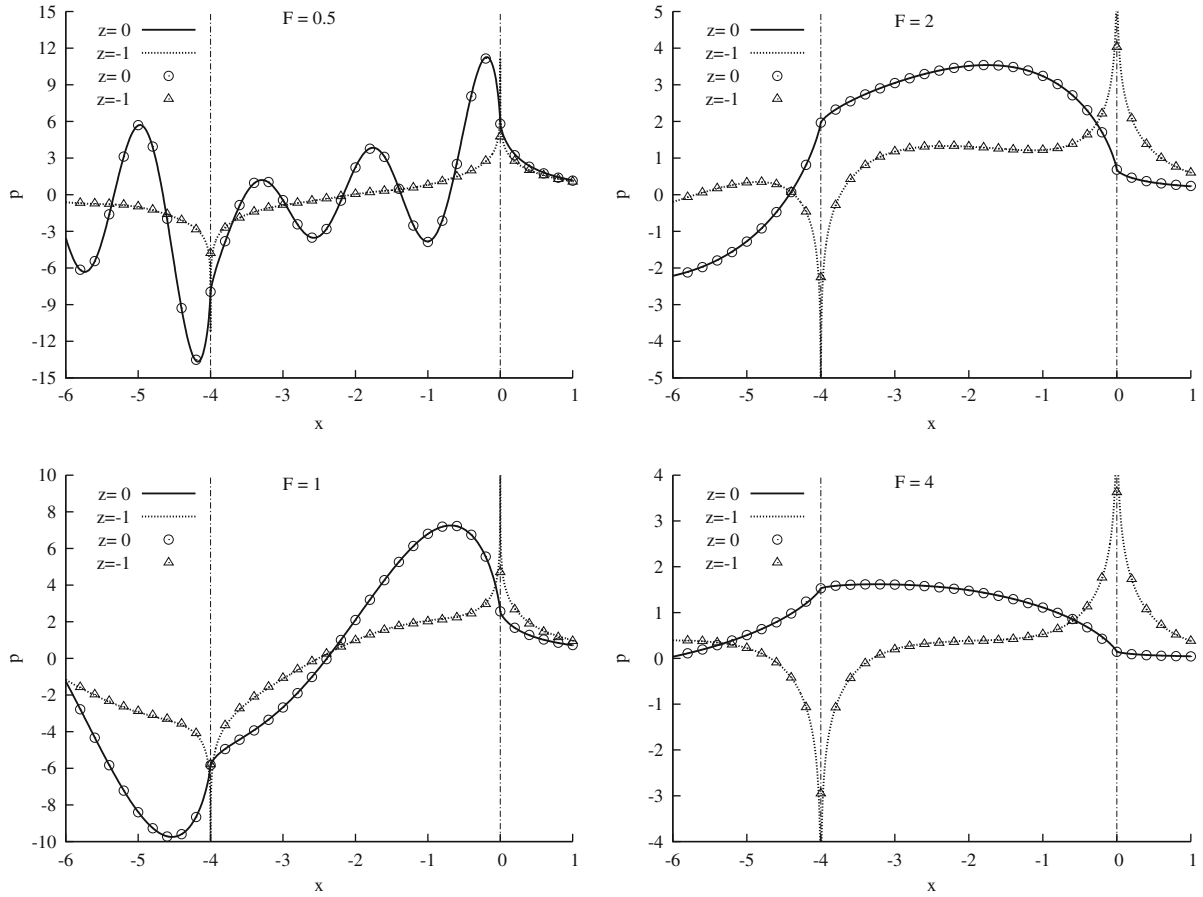

Fig. 15 Pressures $\widetilde{p}^W + \widetilde{p}_a^{SL} + \widetilde{p}_r^L$ (lines) and $\widetilde{p}^W + \widetilde{p}_a^{SL}$ (circles or triangles) for $-6 \le \widetilde{x} \le 1$ at the top waterline $\widetilde{z} = 0$ (for which $\widetilde{p}$ is identical to the free-surface elevation $\widetilde{e}$) and the bottom waterline $\widetilde{z} = -1$ for a wedge-shaped bow between the vertical lines $x = 0$ and $x = -4$

Expressions (5) and (12) yield

$$\widetilde{p}^W = \frac{-4}{\pi F^2} \int_0^\infty \mathrm{d}t \sqrt{1+t^2}\, \mathrm{e}^{(1+t^2)\widetilde{z}/F^2} (C_* \widetilde{C} + S_* \widetilde{S}) \quad \text{with} \quad \begin{Bmatrix} \widetilde{C} \\ \widetilde{S} \end{Bmatrix} \equiv \begin{Bmatrix} \cos(\sqrt{1+t^2}\widetilde{x}/F^2) \\ \sin(\sqrt{1+t^2}\widetilde{x}/F^2) \end{Bmatrix} \tag{29a}$$

and

$$\begin{Bmatrix} C_* \\ S_* \end{Bmatrix} \equiv \frac{1}{F^2} \int\!\!\int_{\widetilde{H}_0} \mathrm{d}x \mathrm{d}z\, \frac{\partial b(x,z)}{\partial x} \mathrm{e}^{z(1+t^2)/F^2} \begin{Bmatrix} \cos(\sqrt{1+t^2}x/F^2) \\ \sin(\sqrt{1+t^2}x/F^2) \end{Bmatrix}. \tag{29b}$$

An alternative expression for $\widetilde{p}^W$ is

$$\widetilde{p}^W = \frac{-4}{\pi F^2} \int_0^\infty \mathrm{d}t \sqrt{1+t^2}\, \mathrm{e}^{(1+t^2)\widetilde{z}/F^2} S(t\,;\widetilde{x}) \tag{29c}$$

with

$$S(t\,;\widetilde{x}) \equiv \frac{1}{F^2} \int\!\!\int_{\widetilde{H}_0} \mathrm{d}x \mathrm{d}z\, \frac{\partial b(x,z)}{\partial x} \mathrm{e}^{z(1+t^2)/F^2} \cos[\sqrt{1+t^2}(x-\widetilde{x})/F^2]. \tag{29d}$$

$\widetilde{H}_0$ in (29b) and (29d) stands for the portion $\widetilde{x} \le x$ of the hull centerplane H_0, in accordance with the unit-step function $H(x-\widetilde{x})$ in (12). The wave component $\widetilde{e}^W$ in (28) is given by the foregoing alternative expressions with $\widetilde{z}=0$ in (29a) or (29c). The wave drag D^W can be determined from the energy radiated by the farfield waves using the Havelock formula

$$C^W \equiv \frac{D^W}{\rho V_s^2 L_{\text{ref}}^2} = \frac{4}{\pi}\int_0^\infty \mathrm{d}t\sqrt{1+t^2}\,(C_*^2+S_*^2), \tag{29e}$$

where C_* and S_* are given by (29b) with $\widetilde{H}_0$ taken as H_0.

Expressions (5) and (23) yield

$$\widetilde{p}_a^{SL} = \frac{1}{2\pi}\int\!\!\int_{H_0} \mathrm{d}x\mathrm{d}z \frac{\partial b(x,z)}{\partial x}\left[|x-\widetilde{x}|M + \frac{2F^2\psi}{(F^2+r_1)^3}\left(1+4.6\,\psi+\frac{F^2}{r_1}\right)\right]\mathrm{sign}(x-\widetilde{x}) \tag{30a}$$

with

$$M \equiv \frac{1}{r^3}-\frac{1}{r_1^3}+\frac{2}{(F^2+r_1)^3}\left[1+\frac{F^2}{r_1}\left(1+2\psi-2.3\,\psi^2\frac{F^2-2r_1}{F^2+r_1}\right)\right], \tag{30b}$$

$$r \equiv \sqrt{(x-\widetilde{x})^2+(z-\widetilde{z})^2}, \quad r_1 \equiv \sqrt{(x-\widetilde{x})^2+(z+\widetilde{z})^2} \tag{30c}$$

and

$$\psi \equiv -(z+\widetilde{z})/(r_1+|x-\widetilde{x}|). \tag{30d}$$

The local-flow component $\widetilde{e}_a^{SL}$ in (28) is given by (30) with $\widetilde{z}=0$, which yields $1/r^3-1/r_1^3=0$ in (30b).

The terms $1/r^3$ and $1/r_1^3$ in (30b) and the term F^2/r_1 in (30a) and (30b) are singular for $r=0$ or $r_1=0$. These singularities can be integrated analytically. In particular, the integral

$$I_p(\widetilde{x},\widetilde{z}) \equiv \int\!\!\int_{H_p} \mathrm{d}x\mathrm{d}z \frac{x-\widetilde{x}}{r^3},$$

where H_p stands for a flat panel bounded by straight segments, can be evaluated using well-known analytical expressions. It is also well known that the integral I_p is null for a flow-field point $(\widetilde{x},\widetilde{z})$ located at the centroid $(\widetilde{x}_p,\widetilde{z}_p)$ of H_p. Thus, the vicinity of a point $(\widetilde{x},\widetilde{z})$ of H_0 only yields a small contribution to the integral

$$\int\!\!\int_{H_0} \mathrm{d}x\mathrm{d}z \frac{\partial b(x,z)}{\partial x}\,\frac{x-\widetilde{x}}{r^3}.$$

This property suggests that a straightforward alternative to analytical integration of the singular terms $1/r^3-1/r_1^3$ in (30b) and F^2/r_1 in (30a) and (30b) consists in performing the substitutions

$$\frac{1}{r^3}-\frac{1}{r_1^3} \to \frac{1}{r^3+\varepsilon}-\frac{1}{r_1^3+\varepsilon_1}, \qquad \frac{1}{r_1} \to \frac{1}{\sqrt{r_1^2+\varepsilon'}}, \tag{31a}$$

where ε, ε_1 and ε' stand for small positive real numbers. These may be taken as

$$\varepsilon = h_p^6/(h_p^3+r^3), \quad \varepsilon_1 = h_p^6/(h_p^3+r_1^3), \quad \varepsilon' = h_p^6/(h_p^4+r_1^4). \tag{31b}$$

Here, h_p is a small positive real number that is related to the size of the elements H_p used to perform the surface integrations over the ship centerplane H_0 in (30a). Expressions (31) show that differences between the functions $1/(r^3+\varepsilon)$ and $1/r^3$ and the functions $1/\sqrt{r_1^2+\varepsilon'}$ and $1/r_1$ are smaller than approximately 1.5% for $2h_p<r$ and 0.14% for $3h_p<r$. The modified integrand of (30a) associated with the substitutions (31a) is a continuous (non-singular) function, like the integrands of (29b) or (29d). Thus, the surface integrals (30a) and (29b) or (29d) can be evaluated using straighforward numerical-integration formulae. In particular, the hull centerplane H_0 can be

divided into a set of elements H_p, e.g. triangular elements, and integration over each element H_p can be performed using a Gaussian rule, e.g. the 7-point quadrature rule for a triangle [19].

The wave drag—already given by the Havelock formula (29e) for the energy radiated by the farfield waves—can also be determined via integration of the pressure over the ship hull. This alternative 'nearfield approach' defines the wave drag as

$$C^W \equiv \frac{D^W}{\rho V_s^2 L_{\text{ref}}^2} = -2 \int\int_{H_0} \mathrm{d}\widetilde{x}\, \mathrm{d}\widetilde{z}\, \frac{\partial b(\widetilde{x},\widetilde{z})}{\partial \widetilde{x}}\, p_a(\widetilde{x},\widetilde{z}), \tag{32a}$$

where $p_a(\widetilde{x},\widetilde{z})$ is the pressure $\widetilde{p}_a$ given by (28)–(31). The hydrodynamic lift F^Z and pitch moment M^Y exerted by the flowing water upon the ship hull are given by the analogous expressions

$$C^L \equiv \frac{F^Z}{\rho V_s^2 L_{\text{ref}}^2} = 2 \int\int_{H_0} \mathrm{d}\widetilde{x}\, \mathrm{d}\widetilde{z}\, \frac{\partial b(\widetilde{x},\widetilde{z})}{\partial \widetilde{z}}\, p_a(\widetilde{x},\widetilde{z}), \tag{32b}$$

$$C^M \equiv \frac{M^Y}{\rho V_s^2 L_{\text{ref}}^3} = -2 \int\int_{H_0} \mathrm{d}\widetilde{x}\, \mathrm{d}\widetilde{z} \left(\widetilde{x}\, \frac{\partial b(\widetilde{x},\widetilde{z})}{\partial \widetilde{z}} - \widetilde{z}\, \frac{\partial b(\widetilde{x},\widetilde{z})}{\partial \widetilde{x}} \right) p_a(\widetilde{x},\widetilde{z}). \tag{32c}$$

The related sinkage h and trim angle t are given by

$$h \equiv \Delta Z / L_{\text{ref}} \approx -F^2 C^L / a_0^W, \quad t \approx -F^2 C^M / a_2^W, \tag{32d}$$

where $a_0^W \equiv A_0^W / L_{\text{ref}}^2$ and $a_2^W \equiv A_2^W / L_{\text{ref}}^4$ stand for the nondimensional area and moment of inertia, with respect to the x axis, of the waterplane of the ship at rest. Specifically, we have

$$a_0^W = 2 \int_{x^S}^{x^B} \mathrm{d}x\, b(x, z=0), \quad a_2^W = 2 \int_{x^S}^{x^B} \mathrm{d}x x^2 b(x, z=0), \tag{32e}$$

where $2b(x, z=0)$ is the local beam at the top waterline $z = 0$, and x^S and x^B stand for the x coordinates of the ship stern and bow, respectively. In (32d), a positive sinkage $0 < h$ and a positive trim angle $0 < t$ correspond to a downward displacement and a bow-up rotation of the ship hull, respectively. Furthermore, expression (32d) for the trim angle t presumes that the origin of the system of coordinates is taken at the centroid of the waterplane of the ship at rest.

Figure 15 shows the pressure $\widetilde{p}^W + \widetilde{p}_a^{SL} + \widetilde{p}_r^L$, evaluated as in the previous section and already depicted in Fig. 14, for $-6 \le \widetilde{x} \le 1$ at the top waterline $\widetilde{z} = 0$ (for which $\widetilde{p}$ is identical to the free-surface elevation $\widetilde{e}$) and the bottom waterline $\widetilde{z} = -1$. Figure 15 also shows the pressure $\widetilde{p}^W + \widetilde{p}_a^{SL}$ evaluated using (28)–(31), and multiplied by $2\pi / \tan\alpha$ in accordance with (26). The wedge-shaped bow considered here is located between the vertical lines $x = 0$ and $x = -4$ shown in Fig. 15. Four draft-based Froude numbers are considered: $F = 0.5$ (top left corner), $F = 1$ (bottom left), $F = 2$ (top right) and $F = 4$ (bottom right). The pressure $\widetilde{p}^W + \widetilde{p}_a^{SL} + \widetilde{p}_r^L$ and the related approximation $\widetilde{p}^W + \widetilde{p}_a^{SL}$, respectively identified by lines or symbols (circles or triangles) in Fig. 15, cannot be distinguished, except for $x = 0$ and $x = -4$. Specifically, the logarithmic singularities at $x = 0$ and $x = -4$ associated with the singular terms $1/r$ and $1/r_1$ in (27b) do not occur in (30). Figure 15 shows that the remainder G_r^L in (22) can be neglected, as already verified in Fig. 14, and that the singular terms $1/r^3$ and $1/r_1^3$ in (30b) and the term F^2/r_1 in (30a) and (30b) can be regularized in accordance with (31).

A uniform distribution of triangular panels is used in the calculations reported in Fig. 15. Specifically, the bow region $-4 \le x \le 0$, $-1 \le z \le 0$ is divided into 80 vertical strips of constant width $\Delta x = 0.05$ and 20 horizontal strips of constant height $\Delta z = 0.05$, i.e., 1600 squares and 3200 triangles. The small positive real number h_p in (31b) is taken as $h_p = C\sigma$ where $\sigma = 0.05$ stands for the size of the triangular panels. Two values of the ratio $C \equiv h_p/\sigma$ equal to 2 and 1 were considered. No difference can be observed among the numerical predictions for $C = 2$ and $C = 1$ except in the vicinities of $x = 0$ and $x = -4$, where smaller values of C yield results that

more closely approach the logarithmic singularity associated with the singular terms $1/r$ and $1/r_1$ in (27b). The calculations reported in Fig. 15 correspond to $C = 1$.

Expressions (28)–(32) provide a practical basis for evaluating the pressure at the hull of a thin ship, the free-surface elevation along the ship hull (and path), the wave drag, the hydrodynamic lift and pitch moment, and the related sinkage and trim experienced by the moving ship. The Fourier integral (29a) and the integrals (30a) and (29b) or (29d) only involve continuous elementary (trigonometric and algebraic) functions of real arguments that can be integrated in a straightforward and efficient way. In particular, the hull centerplane H_0 can be divided into a set of elements H_p, e.g. triangular elements. The pressure $\widetilde{p}$ can then be evaluated at the vertices of the triangles, and integration over each triangle H_p can be performed using a straightforward quadrature rule, e.g. the 7-point rule [19]. For a nonuniform discretization of the ship centerplane H_0 into triangular elements H_p, the small positive real number h_p in (31b) can be taken equal to the average size of the triangular elements that surround the vertex of the particular triangle where $\widetilde{p}$ is evaluated.

10 Application to the Wigley hull

For purposes of illustration, (28)–(32) are now applied to the Wigley hull, for which the local beam b is given by

$$b(x, z) = (1 - 4x^2)(1 - 256z^2)/20 \quad \text{with} \quad -1/2 \le x \le 1/2 \quad \text{and} \quad -1/16 \le z \le 0.$$

Here, the reference length L_{ref} is chosen as the length L_s of the Wigley hull. The centerplane H_0 of the Wigley hull is divided into 140 vertical strips of equal width $\Delta x \approx 0.007$ and 10 horizontal strips of constant height $\Delta z = 0.006$, i.e., 1400 squares and 2800 triangles.

Figure 16 depicts the elevation $e \equiv Eg/V_s^2$ of the wave profile predicted by thin-ship theory (solid line) and measured (square symbols) at the University of Tokyo [20, 21] for the Wigley hull at six Froude numbers $F = 0.25$, 0.267, 0.289, 0.316, 0.354 and 0.408. Figure 16 shows that the bow wave height e_b^{theory} predicted by thin-ship theory is lower than the measured height e_b^{exp}, notably at higher Froude numbers F. The measured and predicted heights e_b^{exp} and e_b^{theory} of the bow waves in Fig. 16, and the corresponding relative differences, are approximately equal to

F	0.25	0.267	0.289	0.316	0.354	0.408
e_b^{exp}	0.20	0.18	0.17	0.16	0.15	0.14
e_b^{theory}	0.174	0.162	0.149	0.134	0.117	0.099
diff	−13 %	−10 %	−12%	−16 %	−22%	−30 %

Thus, for a fine ship bow, thin-ship theory may be expected to underpredict the height of the bow wave by approximately 10% to 30% for Froude numbers in the range $0.25 \le F \le 0.4$. Figure 16 also shows that the thin-ship wave profile is more oscillatory than the measured profile. Furthermore, phase differences between the thin-ship and measured wave profiles can be observed.

Figure 17 shows the wave drag coefficient

$$C_W \equiv \frac{D^W}{\rho\, V_s^2 A^H/2} \equiv C^W \frac{L_{\text{ref}}^2}{A^H/2},$$

where A^H stands for the wetted area of the Wigley hull, measured at the University of Tokyo and the Ship Research Institute [20, 21] and predicted by thin-ship theory (comparisons between theoretical predictions and experimental measurements of wave drag are affected by issues related to the experimental determination of the wave drag in a viscous fluid, as well known) using both the farfield Havelock relation (29e) and the nearfield pressure-integration formula (32a). These alternative theoretical predictions cannot be distinguished in Fig. 17. The wave drag predicted by thin-ship theory is considerably more oscillatory than the measured wave drag, and we can observe significant phase differences between the theoretical and experimental wave-drag curves. The left and right sides of Fig. 18 show the sinkage and trim given by (32b)–(32e) and measured [20, 21]. The sinkage predicted by thin-ship theory is in excellent agreement with measurements. Thin-ship theory also predicts that the trim is small for $F < 0.35$ but

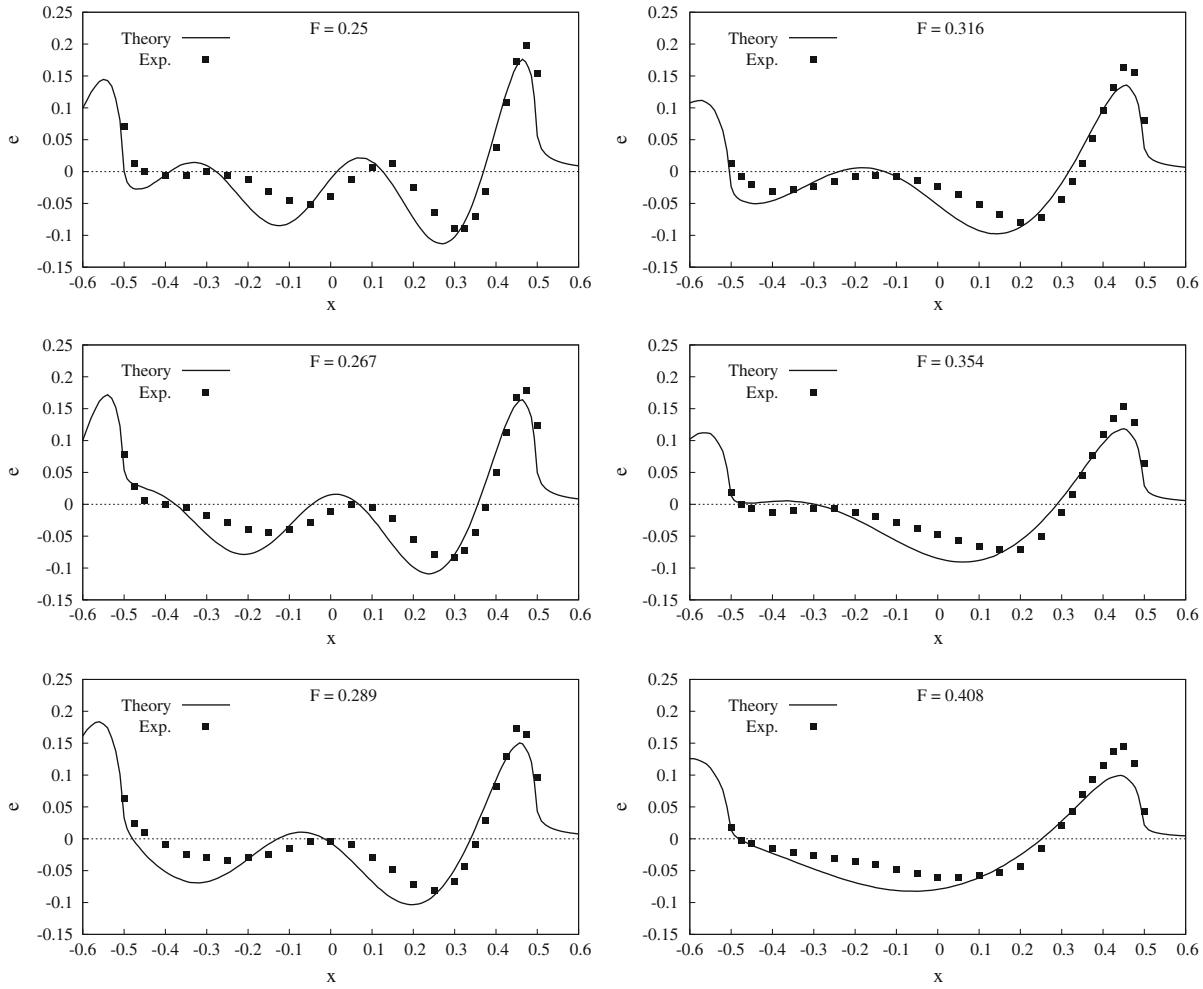

Fig. 16 Elevation $e \equiv E\,g/V_s^2$ of the wave profile predicted by thin-ship theory (solid line) and measured (square symbols) at the University of Tokyo for the Wigley hull at six Froude numbers $F = 0.25, 0.267, 0.289, 0.316, 0.354$ and 0.408

increases rapidly for $0.35 < F$, in agreement with measurements. The limitations of thin-ship theory displayed in Figs. 16–18 are well known and well documented in the literature, e.g. [8–10].

11 Bow waves generated by wedge-shaped ship bows

The two-parameter family of wedge-shaped ship bows considered in [1] corresponds to the special case $\ell = \infty$. This special case is now considered further for $\widetilde{z} = 0$, for which we have $\widetilde{p} \equiv \widetilde{e}$. In the limit $\ell = \infty$, we have $\widetilde{S}_\ell = 0$ in (27a) and the contribution for $x = -\ell$ in (27b) is null. The simple Green function $G_a \equiv G^W + G_a^{SL}$ given by (25), (23) and (12) is used. Thus, (27a) and (27b) yield

$$\frac{\widetilde{e}_a}{2\pi} \approx \frac{\widetilde{e}^W + \widetilde{e}_a^{SL}}{2\pi} = -\frac{4}{\pi}\int_0^\infty \mathrm{d}t\,\frac{1-\mathrm{e}^{-(1+t^2)/F^2}}{1+t^2}\sin(\sqrt{1+t^2}\widetilde{x}/F^2)$$
$$+\frac{1}{\pi}\int_{-1}^{0}\frac{\mathrm{d}z}{F^2+r_1}\left[1+\frac{F^2\psi}{F^2+r_1}\left(1+\frac{2.3\,\psi r_1}{F^2+r_1}\right)\right] \tag{33}$$

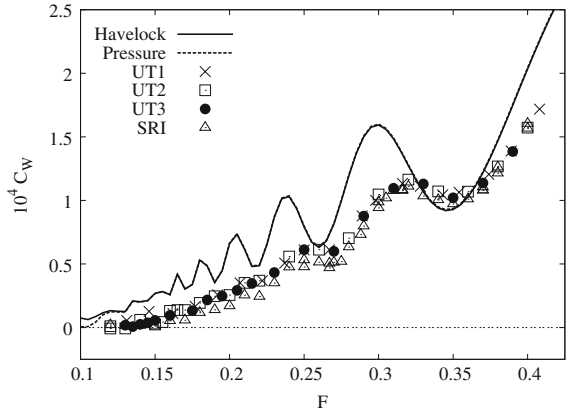

Fig. 17 Wave-resistance coefficient C_W measured at the University of Tokyo and the Ship Research Institute, and predicted by thin-ship theory using the farfield Havelock relation (29e) and the nearfield pressure-integration formula (32a)

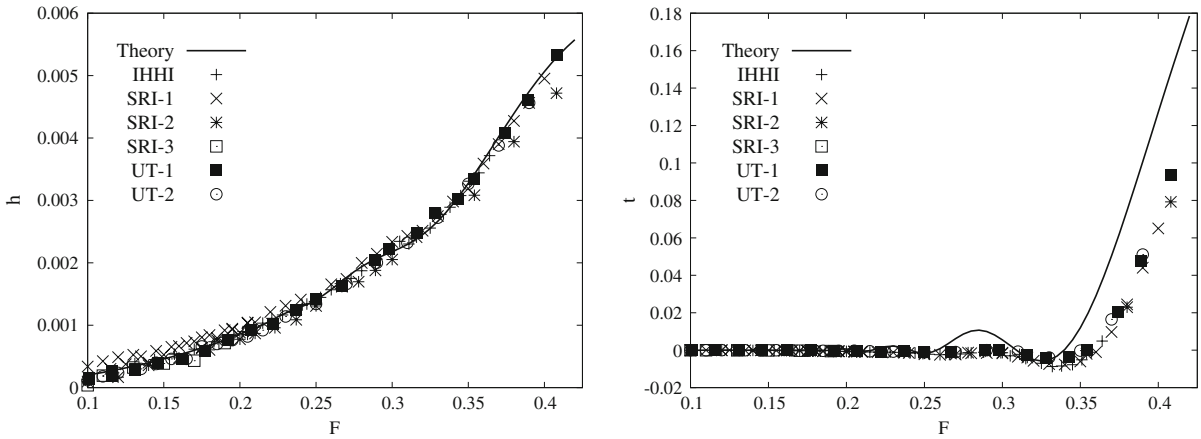

Fig. 18 Experimental measurements and predictions given by thin-ship theory of the sinkage $h \equiv \Delta Z/L_{\text{ref}}$ and trim t for the Wigley hull

with $r_1 = \sqrt{z^2 + \widetilde{x}^2}$ and $\psi = -z/(r_1 + |\widetilde{x}|)$. The free-surface elevation $\widetilde{e}_a/(2\pi)$ given by (33) is depicted in Fig. 19 as a function of $x/F^2 \equiv Xg/V_s^2$ for $F/(1+F) = 0.1, 0.2, \ldots, 0.9$. Figure 20 depicts the free-surface elevation $(1+F)\widetilde{e}_a/(2\pi)$ as a function of $(1+F)x/F^2$, as suggested by the approximations

$$\frac{Z_b\, g/V_s^2}{\tan\alpha} \approx \frac{2.2}{1+F}, \quad -X_b\, g/V_s^2 \approx \frac{1.1}{1+F}, \tag{34}$$

given in [1]. Here, Z_b and $-X_b$ stand for the elevation and the location of the bow wave crest.

The thin-ship theory predictions of the height $(Z_b\, g/V_s^2)/\tan\alpha$ and the location $-X_b\, g/V_s^2$ of the bow wave are shown in Figs. 21 and 22, respectively, as functions of $F/(1+F)$. These predictions of the bow-wave height and location are determined by numerically finding the crest of the bow waves (like those depicted in Fig. 20) predicted by thin-ship theory for every value of the (draft-based) Froude number F. Figures 21 and 22 also show the simple approximations (34), obtained in [1] using fundamental considerations (dimensional analysis and elementary asymptotic considerations) and experimental measurements (for wedge-shaped bows and a rectangular flat plate). Several sets of experimental measurements for wedge-shaped ship bows considered in [1] are also shown in Figs. 21 and 22.

The ratios $Z_b^{\text{thin}}/Z_b^{\text{data}}$ and $X_b^{\text{thin}}/X_b^{\text{data}}$ of the bow-wave heights Z_b and locations $-X_b$ predicted by thin-ship theory and the simple expressions (34) based on experimental data are depicted in Fig. 23 for $0 < F/(1+F) < 1$. The region $0.3 \le F/(1+F) \le 0.7$ between the two vertical lines shown in this figure approximately corresponds to the range $0.4 \le F \le 2.3$. For a typical ship with length/draft ratio $L_s/D \approx 20$, this range approximately corresponds to length-based Froude numbers F_L in the range $0.09 \le F_L \le 0.56$, for which wavemaking is significant.

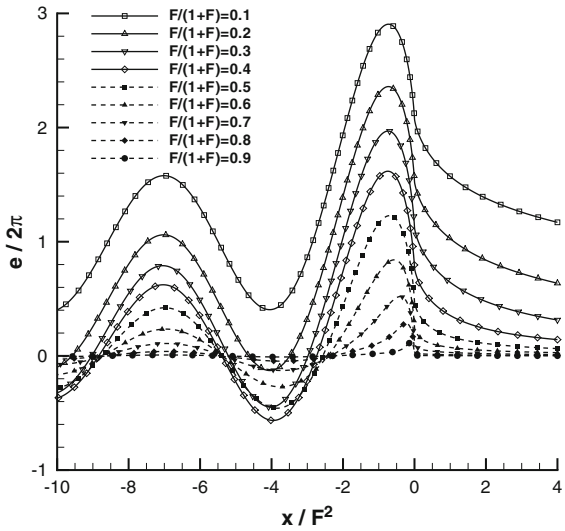

Fig. 19 Free-surface elevation $\widetilde{e}_a/(2\pi)$ as a function of $x/F^2 \equiv X_g/V_s^2$ for wedge-shaped bows without rake or flare

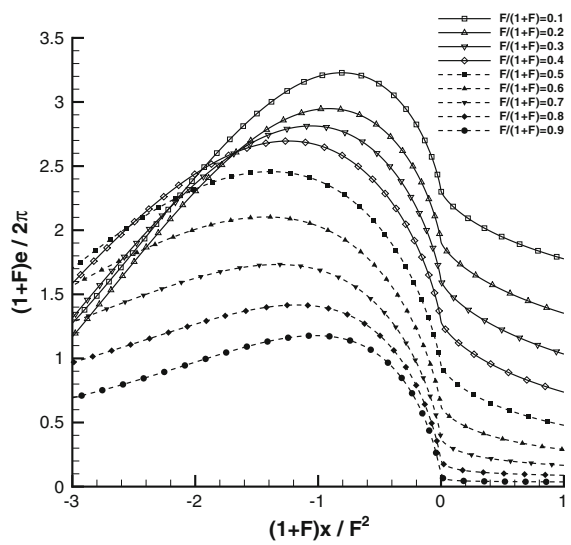

Fig. 20 Free-surface elevation $(1+F)\widetilde{e}_a/(2\pi)$ as a function of $(1+F)x/F^2$ for wedge-shaped bows without rake or flare

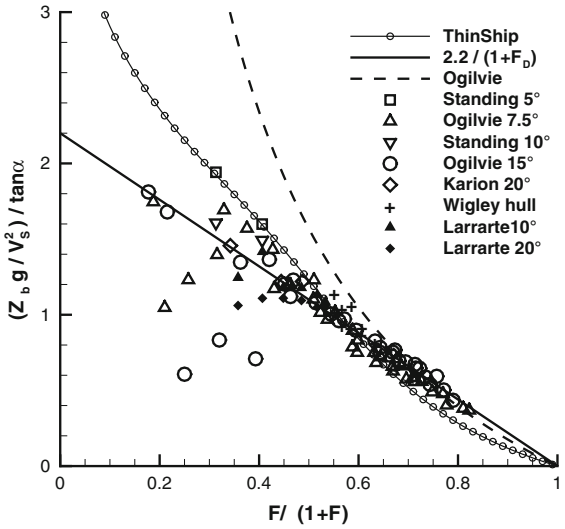

Fig. 21 Bow wave height $(gZ_b/V_s^2)/\tan\alpha$ given by (34) or by thin-ship theory for wedge-shaped bows without rake or flare

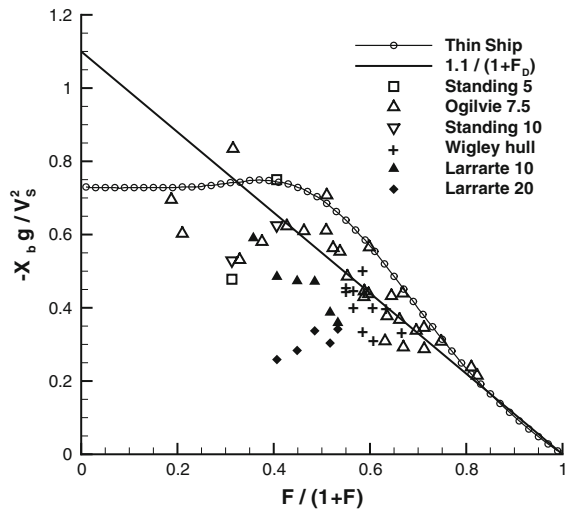

Fig. 22 Location $(-X_b\, g/V_s^2)$ of bow wave crest given by (34) or by thin-ship theory for wedge-shaped bows without rake or flare

Figure 23 shows that, within this 'wavemaking regime', the ratios $Z_b^{\text{thin}}/Z_b^{\text{data}}$ and $X_b^{\text{thin}}/X_b^{\text{data}}$ are approximately comprised between 0.8 and 1.3. For a fine wedge-shaped ship bow, differences between the bow-wave heights and locations predicted by thin-ship theory and the data-based expressions (34) then vary approximately within the range $\pm 25\%$. Thus, for many practical purposes, notably for our purpose and for concept and preliminary design, thin-ship theory is a reasonable and useful approximation, as well documented in the literature, e.g. [5–10]. The ratios $Z_b^{\text{thin}}/Z_b^{\text{data}}$ and $X_b^{\text{thin}}/X_b^{\text{data}}$ are also listed below

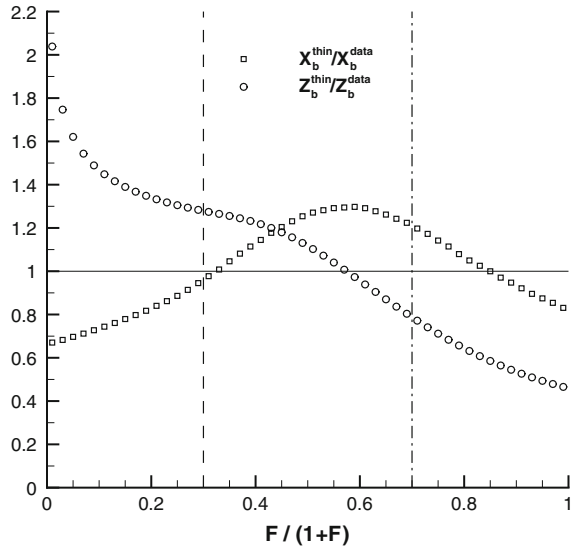

Fig. 23 Ratios $Z_b^{\text{thin}}/Z_b^{\text{data}}$ and $X_b^{\text{thin}}/X_b^{\text{data}}$ of the bow-wave heights Z_b and locations X_b predicted by thin-ship theory and the analytical relations (34) based on experimental data

$F/(1+F)$	0.3	0.4	0.5	0.6	0.7	0.8
$Z_b^{\text{thin}}/Z_b^{\text{data}}$	1.28	1.23	1.12	0.96	0.79	0.64
$X_b^{\text{thin}}/X_b^{\text{data}}$	0.96	1.13	1.26	1.29	1.21	1.07

for $0.3 \le F/(1+F) \le 0.8$, which approximately corresponds to $0.1 \le F_L \le 0.9$ for typical ships with length/draft ratio $L_s/D \approx 20$. Figure 23 and the related foregoing table, and the bow waves shown in Fig. 16, provide an indication of the accuracy that can reasonably be expected from thin-ship theory, and also provide a basis for roughly correcting bow-wave predictions given by thin-ship theory.

12 Application to ruled ship bows with rake and flare

Thin-ship theory is now used to evaluate steady flow about a fine ship bow with rake and flare. Specifically, a ruled ship bow of draft D and semi-infinite length is considered, as illustrated in Fig. 24. The draft D of the bow is chosen as reference length L_{ref} in (1) and (2). The Froude number is then given by $F \equiv V_s/\sqrt{gD}$ (the draft-based Froude number). The hull centerplane H_0 consists of the semi-infinite rectangular region $-\infty \le x \le 0$, $-1 \le z \le 0$. The hull bottom is flat and contained in the horizontal plane $z = -1$. The ship stem intersects the ship centerplane $y = 0$ along the straight line $x = \mu z$ with $-1 \le z \le 0$ and

$$\mu \equiv \tan\delta. \tag{35}$$

Here, δ stands for the rake angle, which can be positive or negative, as shown in Fig. 24. The hull sides intersect the mean free surface $z = 0$ and the hull bottom $z = -1$ along the straight lines $y = \pm\sigma x$ with $x \le 0$, and $y = \pm\sigma'(x+\mu)$ with $x \le -\mu$, respectively. Here, σ and σ' are defined as

$$\sigma \equiv \tan\alpha \quad \sigma' \equiv \tan\alpha' \tag{36}$$

where 2α and $2\alpha'$ stand for the entrance angles of the waterlines at the mean free surface $z = 0$ and at the hull bottom $z = -1$, respectively. The hull sides are defined by $y = \pm b(x, z)$ where

$$b(x,z) = -[\sigma(1+z) - \sigma' z](x - \mu z) \quad \text{with} \quad x \le \mu z \quad \text{and} \quad -1 \le z \le 0. \tag{37}$$

Expressions (37) define a family of ship hulls that depend on four parameters: the top-waterline half entrance angle α, the bottom-waterline half entrance angle α', the rake angle δ, and the draft D. Steady flow about this four-parameter family of ship hulls similarly depends on four parameters: α, α', δ, and the draft-based Froude number F. Figure 1 shows the hulls defined by (37) with $\delta = 45°$, $\alpha = 15°$, $\alpha' = 5°$ or $\delta = -45°$, $\alpha = 5°$, $\alpha' = 15°$.

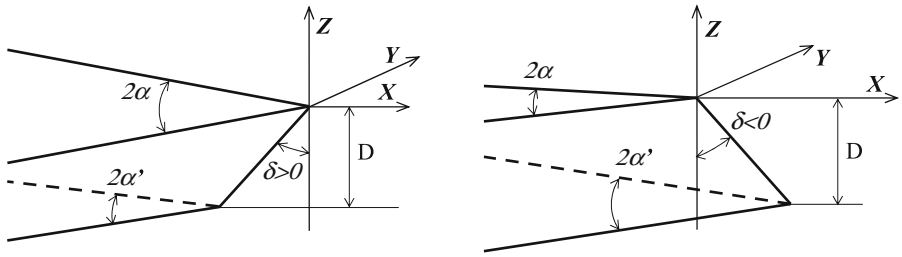

Fig. 24 Four-parameter family of ship bows defined by the draft D, the top-waterline entrance angle 2α, the bottom-waterline entrance angle $2\alpha'$, and the rake angle δ

The slope b_x of the hull (37) is given by $-b_x = \sigma + (\sigma - \sigma')z$ with $x \le \mu z$ and $-1 \le z \le 0$. Expression (5) then yields

$$\widetilde{p} = -2\int_{-1}^{0} \mathrm{d}z \int_{-\infty}^{\mu z} \mathrm{d}x\, [\sigma + (\sigma - \sigma')z]\frac{\partial G}{\partial x} = -2\int_{-1}^{0} \mathrm{d}z\, [\sigma + (\sigma - \sigma')z]\widehat{G}$$

with

$$\widehat{G} \equiv \widehat{G}(z; \widetilde{x}, \widetilde{z}) \equiv G(x = \mu z, 0, z; \widetilde{x}, 0, \widetilde{z}).$$

The simple Green function $G_a \equiv G^W + G_a^{SL}$ given by (25), (23) and (12) is used, in accordance with the results shown in Sect. 8 and depicted in Fig. 14. We then have

$$\widetilde{p} = \sigma\,\widetilde{p}_0 + (\sigma - \sigma')\widetilde{p}_1 \approx \sigma(\widetilde{p}_0^{SL} + \widetilde{p}_0^{W}) + (\sigma - \sigma')(\widetilde{p}_1^{SL} + \widetilde{p}_1^{W}), \tag{38}$$

where the components $(\cdot)^{SL}$ and $(\cdot)^W$ correspond to the local-flow component G_a^{SL} and the wave component G^W in (25) and are defined as

$$\left\{\begin{array}{c} \widetilde{p}_0^{SL} + \widetilde{p}_0^{W} \\ \widetilde{p}_1^{SL} + \widetilde{p}_1^{W} \end{array}\right\} \equiv -2\int_{-1}^{0} \mathrm{d}z \left\{\begin{array}{c} 1 \\ z \end{array}\right\} (\widehat{G}_a^{SL} + \widehat{G}^{W}) \equiv \left\{\begin{array}{c} \widetilde{p}_0 \\ \widetilde{p}_1 \end{array}\right\}. \tag{39}$$

A useful alternative form of (38) is

$$\widetilde{p} = \widehat{\sigma}[\widetilde{p}_0 + \varphi(\widetilde{p}_0 + 2\widetilde{p}_1)] \equiv \widehat{\sigma}\,\widetilde{p}_*, \tag{40}$$

where $\widehat{\sigma}$ and φ are defined as

$$\widehat{\sigma} \equiv \frac{\sigma + \sigma'}{2} \equiv \frac{\tan\alpha + \tan\alpha'}{2}, \quad -1 \le \varphi \equiv \frac{\sigma - \sigma'}{\sigma + \sigma'} \le 1. \tag{41}$$

The parameter $\widehat{\sigma}$ represents an 'average entrance angle', and the parameter φ is associated with the hull flare. We have $\varphi = 1$ if $\alpha' = 0$, $\varphi = 0$ if $\alpha' = \alpha$, and $\varphi = -1$ if $\alpha = 0$. Henceforth the parameter φ is referred to as the hull flare for convenience, although φ is not identical to the flare angle; in fact, a rake angle $\delta \ne 0$ results in flare even if $\varphi = 0$. Thus, the flow under consideration, which depends on the four parameters α, α', δ and F as already noted, is expressed by (40) as the product of the 'average entrance angle' $\widehat{\sigma}$ and the function $\widetilde{p}_*$ that depends on the three variables F, δ and φ. More precisely, the function $\widetilde{p}_*$ is expressed by (40) in terms of the hull flare φ and two functions $\widetilde{p}_0$ and $\widetilde{p}_1$ that depend on the (draft-based) Froude number F and the rake angle δ.

Expressions (39) and (23) yield

$$\left\{\begin{array}{c} \widetilde{p}_0^{SL} \\ \widetilde{p}_1^{SL} \end{array}\right\} = \frac{1}{2\pi}\int_{-1}^{0} \mathrm{d}z \left\{\begin{array}{c} 1 \\ z \end{array}\right\}\left[\frac{1}{r} - \frac{1}{r_1} + \frac{2}{F^2 + r_1} + \frac{2F^2\psi}{(F^2 + r_1)^2}\left(1 + \frac{2.3\psi r_1}{F^2 + r_1}\right)\right] \tag{42a}$$

with

$$r \equiv \sqrt{(\mu z - \widetilde{x})^2 + (z - \widetilde{z})^2}, \quad r_1 \equiv \sqrt{(\mu z - \widetilde{x})^2 + (z + \widetilde{z})^2}, \tag{42b}$$

and

$$\psi \equiv -(z+\widetilde{z})/(r_1 + |\mu z - \widetilde{x}|). \tag{42c}$$

In the special case $\mu = 0$, the function $2\pi\,\widetilde{p}_0^{SL}$ is identical to the function $\widetilde{p}_a^{SL}$ defined by (27b) with $\ell = \infty$.

Expressions (39) and (12) yield

$$\left\{\begin{array}{c}\widetilde{p}_0^W\\ \widetilde{p}_1^W\end{array}\right\} = \frac{-4}{\pi}\int_0^\infty \mathrm{d}t\,\frac{\mathrm{e}^{T^2\widetilde{z}/F^2}}{T}\left\{\begin{array}{c}A_0\\ A_1\end{array}\right\} \quad \text{with} \quad T \equiv \sqrt{1+t^2}, \tag{43}$$

$$\left\{\begin{array}{c}A_0\\ A_1\end{array}\right\} = \Im\mathfrak{m}\,\mathrm{e}^{\mathrm{i}\,T\widetilde{x}/F^2}\left\{\begin{array}{c}I_0\\ I_1\end{array}\right\} \quad \left\{\begin{array}{c}I_0\\ I_1\end{array}\right\} = \frac{T}{F^2}\int_{-1}^0 \mathrm{d}z\left\{\begin{array}{c}1\\ z\end{array}\right\}\mathrm{e}^{(T-\mathrm{i}\mu)Tz/F^2}H(\mu z - \widetilde{x}). \tag{44}$$

The step function $H(\mu z - \widetilde{x})$ in (44) readily yields

$$\left\{\begin{array}{c}\widetilde{p}_0^W\\ \widetilde{p}_1^W\end{array}\right\} = 0 \quad \text{for} \quad \left\{\begin{array}{c}0 \le \widetilde{x}\\ -\mu \le \widetilde{x}\end{array}\right\} \quad \text{if} \quad \left\{\begin{array}{c}0 < \mu\\ \mu < 0\end{array}\right\}, \tag{45}$$

$$\left\{\begin{array}{c}I_0\\ I_1\end{array}\right\} = \frac{T}{F^2}\int_{-1}^0 \mathrm{d}z\left\{\begin{array}{c}1\\ z\end{array}\right\}\mathrm{e}^{(T-\mathrm{i}\,\mu)Tz/F^2} \quad \text{for} \quad \left\{\begin{array}{c}\widetilde{x} \le -\mu\\ \widetilde{x} \le 0\end{array}\right\} \quad \text{if} \quad \left\{\begin{array}{c}0 < \mu\\ \mu < 0\end{array}\right\},$$

$$\left\{\begin{array}{c}I_0\\ I_1\end{array}\right\} = \frac{T}{F^2}\int_{\widetilde{x}/\mu}^0 \mathrm{d}z\left\{\begin{array}{c}1\\ z\end{array}\right\}\mathrm{e}^{(T-\mathrm{i}\mu)Tz/F^2} \quad \text{for} \quad -\mu \le \widetilde{x} \le 0 \quad \text{if} \quad 0 < \mu,$$

$$\left\{\begin{array}{c}I_0\\ I_1\end{array}\right\} = \frac{T}{F^2}\int_{-1}^{\widetilde{x}/\mu} \mathrm{d}z\left\{\begin{array}{c}1\\ z\end{array}\right\}\mathrm{e}^{(T-\mathrm{i}\,\mu)Tz/F^2} \quad \text{for} \quad 0 \le \widetilde{x} \le -\mu \quad \text{if} \quad \mu < 0.$$

These expressions for I_0 and I_1 and the relations

$$\frac{T}{F^2}\int_a^b \mathrm{d}z\,z\,\mathrm{e}^{(T-\mathrm{i}\mu)Tz/F^2} = T_*\left[\mathrm{e}^{(T-\mathrm{i}\mu)Tz/F^2}\left(z - \frac{F^2T_*}{T}\right)\right]_a^b \quad \text{and}$$

$$\frac{T}{F^2}\int_a^b \mathrm{d}z\,\mathrm{e}^{(T-\mathrm{i}\,\mu)Tz/F^2} = T_*\left[\mathrm{e}^{(T-\mathrm{i}\,\mu)Tz/F^2}\right]_a^b \quad \text{with} \quad T_* \equiv \frac{T+\mathrm{i}\,\mu}{T^2+\mu^2}$$

yield

$$I_0 = T_*\left(1 - \mathrm{e}^{-(T-\mathrm{i}\mu)T/F^2}\right) \quad I_1 = T_*\left[\left(\frac{F^2T_*}{T}+1\right)\mathrm{e}^{-(T-\mathrm{i}\mu)T/F^2} - \frac{F^2T_*}{T}\right]$$

for $\widetilde{x} \le -\mu$ if $0 < \mu$ and for $\widetilde{x} \le 0$ if $\mu < 0$,

$$I_0 = T_*\left(1 - \mathrm{e}^{(T/\mu-\mathrm{i})T\widetilde{x}/F^2}\right) \quad I_1 = T_*\left[\left(\frac{F^2T_*}{T} - \frac{\widetilde{x}}{\mu}\right)\mathrm{e}^{(T/\mu-\mathrm{i})T\widetilde{x}/F^2} - \frac{F^2T_*}{T}\right]$$

for $-\mu \le \widetilde{x} \le 0$ if $0 < \mu$,

$$I_0 = T_*\left(\mathrm{e}^{(T/\mu-\mathrm{i})T\widetilde{x}/F^2} - \mathrm{e}^{-(T-\mathrm{i}\mu)T/F^2}\right),$$

$$I_1 = T_*\left[\left(\frac{F^2T_*}{T}+1\right)\mathrm{e}^{-(T-\mathrm{i}\mu)T/F^2} - \left(\frac{F^2T_*}{T}-\frac{\widetilde{x}}{\mu}\right)\mathrm{e}^{(T/\mu-\mathrm{i})T\widetilde{x}/F^2}\right]$$

for $0 \le \widetilde{x} \le -\mu$ if $\mu < 0$.

The foregoing expressions for I_0 and I_1 show that the amplitude functions A_0 and A_1 defined by (44) are given by

$$\left.\begin{aligned} A_0(T^2+\mu^2) &= T(\widetilde{S}-E\widetilde{S}_*)+\mu(\widetilde{C}-E\widetilde{C}_*) \\ A_1(T^2+\mu^2)^2 &= (T^2+\mu^2)\,E(T\widetilde{S}_*+\mu\widetilde{C}_*)+F^2(T-\mu^2/T)(E\widetilde{S}_*-\widetilde{S})+2F^2\mu(E\widetilde{C}_*-\widetilde{C}) \end{aligned}\right\} \tag{46a}$$

for $\widetilde{x} \le -\mu$ if $0 < \mu$ and for $\widetilde{x} \le 0$ if $\mu < 0$, or by

$$\left.\begin{aligned} A_0(T^2+\mu^2) &= T\widetilde{S}+\mu(\widetilde{C}-E_*) \\ A_1(T^2+\mu^2)^2 &= 2F^2\mu(E_*-\widetilde{C})-F^2(T-\mu^2/T)\widetilde{S}-(T^2+\mu^2)\widetilde{x}\,E_* \end{aligned}\right\} \tag{46b}$$

for $-\mu \le \widetilde{x} \le 0$ if $0 < \mu$, or by

$$\left.\begin{aligned} A_0(T^2+\mu^2) &= \mu(E_*-E\widetilde{C}_*)-TE\widetilde{S}_* \\ A_1(T^2+\mu^2)^2 &= F^2(T-\mu^2/T)\,E\widetilde{S}_*+2F^2\mu(E\widetilde{C}_*-E_*) \\ &\quad +(T^2+\mu^2)(T\,E\widetilde{S}_*+\mu E\,\widetilde{C}_*+\widetilde{x}\,E_*) \end{aligned}\right\} \tag{46c}$$

for $0 \le \widetilde{x} \le -\mu$ if $\mu < 0$. In (46a)–(46c), $\widetilde{C}$, $\widetilde{S}$, $\widetilde{C}_*$, $\widetilde{S}_*$, E and E_* stand for the functions

$$\left\{\begin{matrix}\widetilde{C}\\ \widetilde{S}\end{matrix}\right\} = \left\{\begin{matrix}\cos(T\widetilde{x}/F^2)\\ \sin(T\widetilde{x}/F^2)\end{matrix}\right\},\quad \left\{\begin{matrix}\widetilde{C}_*\\ \widetilde{S}_*\end{matrix}\right\} = \left\{\begin{matrix}\cos[T(\widetilde{x}+\mu)/F^2]\\ \sin[T(\widetilde{x}+\mu)/F^2]\end{matrix}\right\},\quad \left\{\begin{matrix}E\\ E_*\end{matrix}\right\} = \left\{\begin{matrix}\exp(-T^2/F^2)\\ \exp[(\widetilde{x}/\mu)T^2/F^2]\end{matrix}\right\}. \tag{46d}$$

In the special case $\mu = 0$, expression (46a) for A_0 yields $A_0 = (1-E)\widetilde{S}/T$ and the function $2\pi\,\widetilde{p}_0^W$ defined by (43) is identical to the function $\widetilde{p}^W$ defined by (27a) with $\ell = -\infty$.

In summary, thin-ship theory, with the simplified Green function given by (25), (23) and (12), shows that the pressure $\widetilde{p}$ at a flow-field point $(\widetilde{x}, 0, \widetilde{z})$ of the four-parameter family of ship hulls (37) is given by (38), (42), (43), (45) and (46).

13 Parametric study of rake and flare effects on bow wave

The free-surface elevation $\widetilde{e}$ along the hull, obtained by setting $\widetilde{z} = 0$ in (42) and (43), is now considered for $0.3 \le F/(1+F) \le 0.8$, $-60° \le \delta \le 60°$ and $-1 \le \varphi \le 1$. The range $0.3 \le F/(1+F) \le 0.8$ approximately corresponds to draft-based Froude numbers F in the range $0.43 \le F \le 4$ and, for a typical ship with length/draft ratio $L_s/D \approx 20$, to length-based Froude numbers F_L in the approximate range $0.1 \le F_L \le 0.9$. This Froude-number range and the ranges $-60° \le \delta \le 60°$ and $-1 \le \varphi \le 1$ encompass most practical cases.

Expressions (40) and (41) yield

$$\widetilde{e} = \frac{\tan\alpha+\tan\alpha'}{2}\,\{\widetilde{p}_0(\widetilde{x}\,;F,\delta)+\varphi[\widetilde{p}_0(\widetilde{x}\,;F,\delta)+2\widetilde{p}_1(\widetilde{x}\,;F,\delta)]\}. \tag{47a}$$

This relation yields

$$\widetilde{e} = \tan\frac{\alpha+\alpha'}{2}\,\widetilde{p}_0(\widetilde{x}\,;F,\delta=0) \quad \text{if } \delta = 0 \quad \text{and} \quad \varphi = 0. \tag{47b}$$

The crest of the bow waves defined by (47a) and (47b) are determined by numerically finding the highest value of the free-surface elevation $\widetilde{e}$. The ratio of the heights of the bow waves defined by (47a) and (47b) is given by

$$\frac{\tan\alpha+\tan\alpha'}{2\tan[(\alpha+\alpha')/2]}\,\zeta_b(F,\delta,\varphi) \tag{48a}$$

with

$$\zeta_b(F,\delta,\varphi) = \frac{\max\{\widetilde{p}_0(\widetilde{x}\,;F,\delta)+\varphi[\widetilde{p}_0(\widetilde{x}\,;F,\delta)+2\widetilde{p}_1(\widetilde{x}\,;F,\delta)]\}}{\max\{\widetilde{p}_0(\widetilde{x}\,;F,\delta=0)\}}. \tag{48b}$$

The locations of the crests of the bow waves (47a) and (47b) are defined by $X_b(F, \delta, \varphi)$ and $X_b(F, \delta = 0, \varphi = 0)$. The function $\zeta_b(F, \delta, \varphi)$ defined by (48b) and the function

$$\xi_b(F, \delta, \varphi) \equiv X_b(F, \delta, \varphi)/X_b(F, \delta = 0, \varphi = 0) \tag{48c}$$

quantify the variations of the bow-wave height Z_b and location $-X_b$ due to the rake angle δ and the hull flare φ. The relations (48) and (34) yield

$$\frac{Z_b\, g}{V_s^2} \approx (\tan\alpha + \tan\alpha')\frac{1.1}{1+F}\zeta_b(F, \delta, \varphi), \quad \frac{-X_b\, g}{V_s^2} \approx \frac{1.1}{1+F}\xi_b(F, \delta, \varphi) \tag{49a}$$

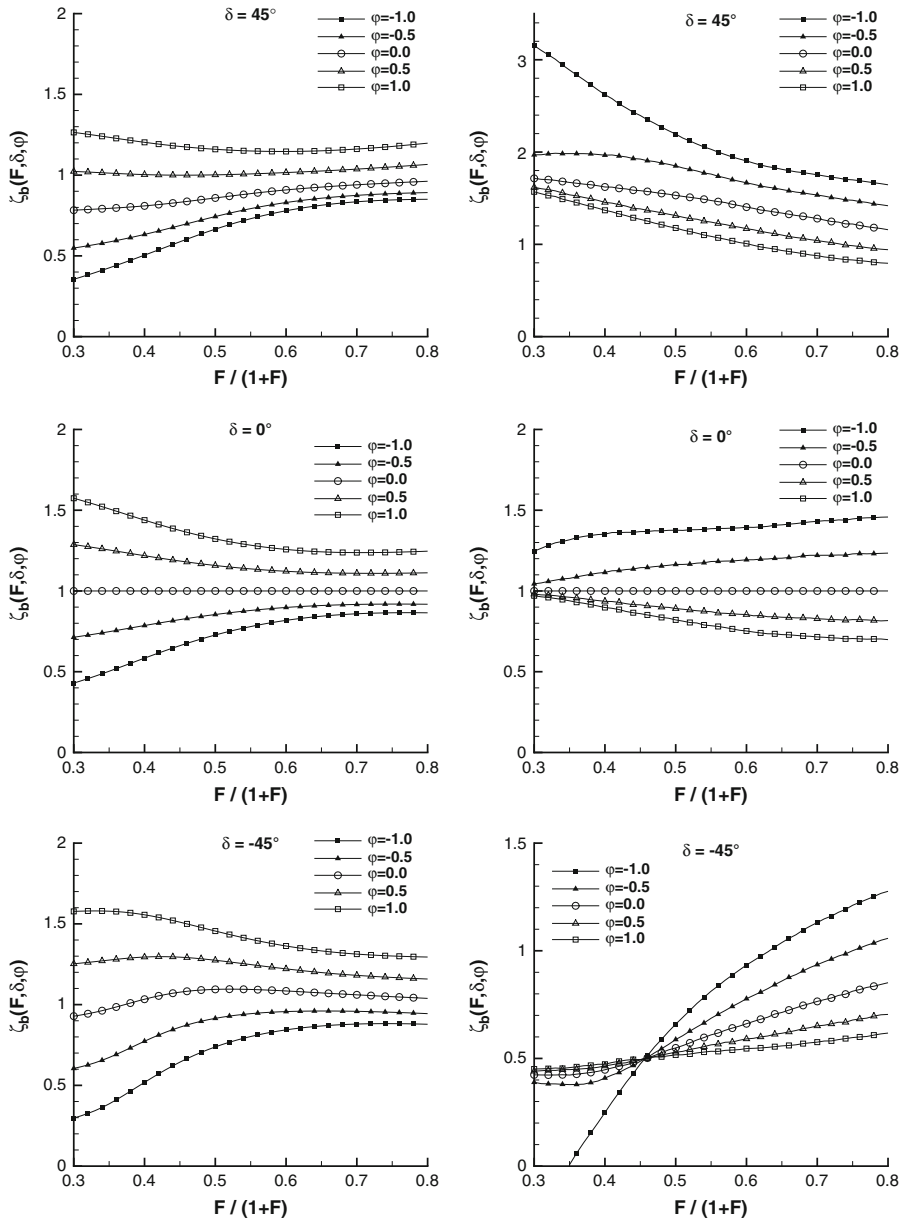

Fig. 25 Variations of the functions ζ_b (left column) and ξ_b (right) defined by (48b) and (48c) with respect to the draft-based Froude number F in the range $0.3 \le F/(1+F) \le 0.8$ for three rake angles $\delta = 45°, 0°, -45°$ (top, center and bottom rows) and five hull flares $\varphi = 1,\ 0.5, 0, -0.5, -1$

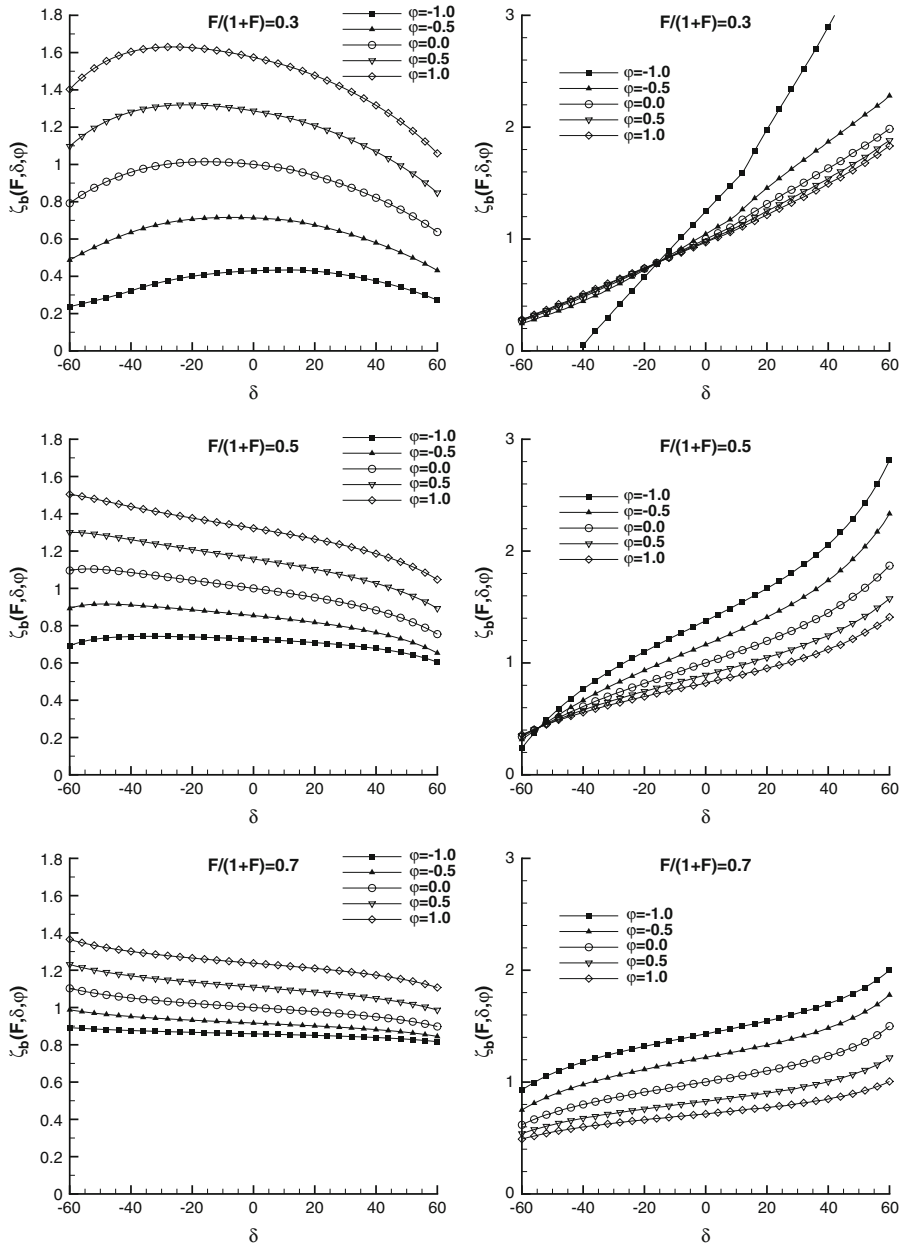

Fig. 26 Variations of the functions ζ_b (left column) and ξ_b (right) defined by (48b) and (48c) with respect to the rake angle $-60° \leq \delta \leq 60°$ for three Froude numbers $F/(1+F) = 0.3, 0.5, 0.7$ (top, center and bottom rows) and five hull flares $\varphi = 1,\ 0.5, 0, -0.5, -1$

with

$$F \equiv \frac{V_s}{\sqrt{g\,D}} \quad \text{and } \varphi \equiv \frac{\tan\alpha - \tan\alpha'}{\tan\alpha + \tan\alpha'}. \tag{49b}$$

In the special case $\delta = 0$ and $\varphi = 0$, we have $\zeta_b = 1$ and $\xi_b = 1$, and (49) and (34) are identical as expected. Expressions (49) account for the effect of the rake angle δ and the flare parameter φ on the bow-wave height Z_b and location $-X_b$ via the functions $\zeta_b(F, \delta, \varphi)$ and $\xi_b(F, \delta, \varphi)$. More precisely, these two functions—determined using thin-ship theory—provide corrections to the relations (34), obtained in [1, 2] using simple fundamental considerations and

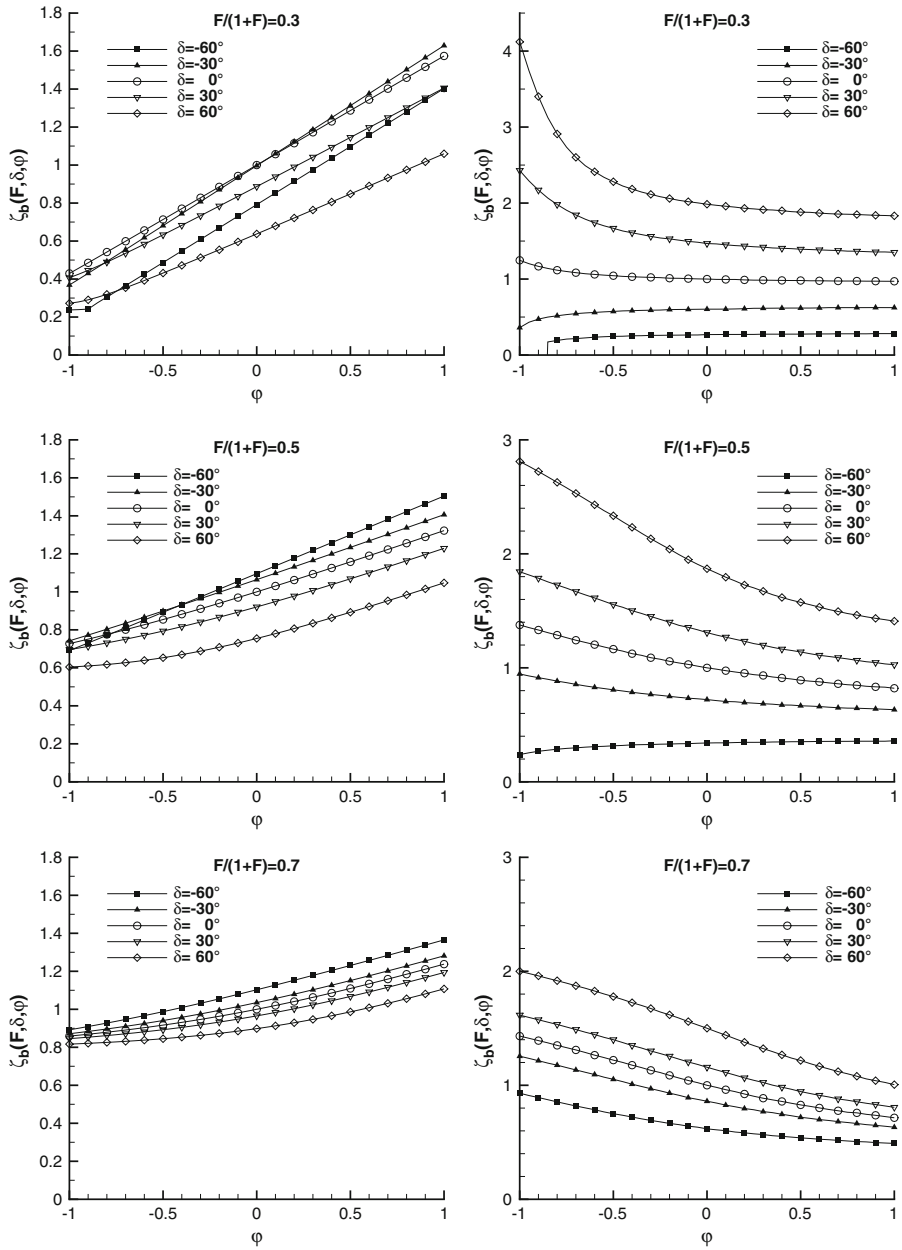

Fig. 27 Variations of the functions ζ_b (left column) and ξ_b (right) defined by (48b) and (48c) with respect to the hull flare $-1 \leq \varphi \leq 1$ for three Froude numbers $F/(1+F) = 0.3, 0.5, 0.7$ (top, center and bottom rows) and five rake angles $\delta = 60°, 30°, 0°, -30°, -60°$

experimental data. The thin-ship corrections for rake and flare provided by the functions ζ_b and ξ_b could also be applied to the bow-wave height and location predicted by thin-ship theory, and depicted in Figs. 21–23. The relations (34) are used in (49) because they are simpler, and because Figs. 21–22 suggest that (34) can be expected to be more accurate—notably for the bow-wave height Z_b—than the thin-ship predictions.

The functions ζ_b and ξ_b defined by (48b) and (48c) are depicted in the left and right columns of Figs. 25–27. Figure 25 shows the variations of the functions ζ_b and ξ_b with respect to the (draft-based) Froude number F in the range $0.3 \leq F/(1+F) \leq 0.8$ for three rake angles $\delta = 45°, 0°, -45°$ (top, center and bottom rows) and five

hull flares $\varphi = 1,\ 0.5, 0, -0.5, -1$. Figure 26 depicts the variations of the functions ζ_b and ξ_b with respect to the rake angle δ in the range $-60^\circ \le \delta \le 60^\circ$ for $F/(1+F) = 0.3, 0.5, 0.7$ (top, center and bottom rows) and five hull flares $\varphi = 1,\ 0.5, 0, -0.5, -1$. Figure 27 similarly depicts the variations of ζ_b and ξ_b with respect to the flare parameter φ in the range $-1 \le \varphi \le 1$ for $F/(1+F) = 0.3, 0.5, 0.7$ (top, center and bottom rows) and five rake angles $\delta = 60^\circ, 30^\circ, 0^\circ, -30^\circ, -60^\circ$.

The values of the functions ζ_b and ξ_b defined by (48b) and (48c) are listed in Tables 1a–f and 2a–f for six values of the draft-based Froude number F that correspond to $F/(1+F) = 0.3, 0.4, \ldots, 0.8$, nine values of the hull flare parameter $\varphi = 1, 0.75, \ldots, -1$ and nine rake angles $\delta = 60^\circ, 45^\circ, \ldots, -60^\circ$. The values of the functions ζ_b and ξ_b for arbitrary values of F, φ and δ in the ranges $0.3 \le F/(1+F) \le 0.8$, $-1 \le \varphi \le 1$, $-60^\circ \le \delta \le 60^\circ$ can be determined via interpolation of the values given in Tables 1a–f and 2a–f. In the special case $\delta = 0$ and $\varphi = 0$, Tables 1a–2f and Figs. 25–27 show that we have $\zeta_b = 1$ and $\xi_b = 1$ as expected. The relations (49) and the 12 Tables 1a–f and 2a–f of values of the functions ζ_b and ξ_b provide estimates—immediately useful for design—of the influence of rake and flare on the height Z_b and the location $-X_b$ of a ship bow wave.

Tables 1a–f and 2a–f and Figs. 25–27 also show that effects of rake and flare can be significant, especially at low Froude numbers. In particular, the left side of Fig. 27 and Table 1a–f show that ζ_b is a monotonically increasing function of the hull flare parameter φ within the range $-1 \le \varphi \le 1$, for every value of the Froude number F and the rake angle δ, as we would intuitively expect. Specifically, Table 1a–f shows that the smallest and largest values $\zeta_b^{\min}$ and $\zeta_b^{\max}$ of ζ_b are attained for $\varphi = -1$ and $\varphi = 1$, respectively, and are equal to

$F/(1+F)$	0.3	0.4	0.5	0.6	0.7	0.8,
$\zeta_b^{\max}$	1.63	1.56	1.50	1.43	1.37	1.33,
$\zeta_b^{\min}$	0.24	0.39	0.60	0.75	0.82	0.84.

These values substantially differ from 1, especially for small values of F. Thus, flare can have significant influence on the height Z_b of a ship bow wave, and this influence clearly is more important at smaller Froude numbers. The right side of Fig. 26 and Table 2a–f show that ξ_b is a monotonically increasing function of the rake angle δ within the range $-60^\circ \le \delta \le 60^\circ$, for every value of the Froude number F and the flare parameter φ, as we would also expect intuitively. Specifically, Table 2a–f shows that the smallest and largest values $\xi_b^{\min}$ and $\xi_b^{\max}$ of ξ_b are attained for $\delta = -60^\circ$ and $\delta = 60^\circ$, respectively, and are equal to

$F/(1+F)$	0.3	0.4	0.5	0.6	0.7	0.8,
$\xi_b^{\max}$	4.12	3.45	2.81	2.30	2.00	1.79,
$\xi_b^{\min}$	−5.50	−1.27	0.24	0.42	0.49	0.56.

These values also substantially differ from 1, especially for small values of F. Rake can then have significant influence on the location $-X_b$ of a ship bow wave, and this influence is more important at smaller Froude numbers.

14 Conclusion

Two practical results, useful for ship design at early stages, have been reported. One of these two results is a straightforward mathematical basis, given by (28)–(32), for numerically evaluating—within the context of the thin-ship theory of steady flow about a ship in deep water—the pressure at the hull of a ship, the free-surface elevation along the ship hull and path, the wave drag, the hydrodynamic lift and pitch moment, and the related sinkage and trim. This mathematical basis only involves continuous elementary (trigonometric and algebraic) functions of real arguments that can be integrated in a straightforward and efficient way using ordinary quadrature rules. A Fortran code based on the mathematical formulation given by (28)–(32) can evaluate the pressure distribution at a ship hull, discretized into 10,000 flat triangles, in less than 10 s per ship speed using a common PC, i.e., fast enough to be of practical use for ship design.

The main ingredient of the flow representation (28)–(32) is a remarkably simple Green function. This 'thin-ship theory' Green function, for which we have $y - \widetilde{y} = 0$, is given by

Table 1 Function $\zeta_b(F, \delta, \varphi)$ defined by (48b) for (**a**) $F/(1+F) = 0.3$, (**b**) $F/(1+F) = 0.4$, (**c**) $F/(1+F) = 0.5$, (**d**) $F/(1+F) = 0.6$, (**e**) $F/(1+F) = 0.7$, and (**f**) $F/(1+F) = 0.8$

$\varphi \downarrow \quad \delta \rightarrow$	60°	45°	30°	15°	0°	−15°	−30°	−45°	−60°
(**a**) $F/(1+F) = 0.3$									
1	1.06	1.26	1.41	1.51	1.57	1.62	1.63	1.58	1.40
0.75	0.95	1.14	1.28	1.37	1.43	1.47	1.47	1.42	1.25
0.5	0.85	1.02	1.15	1.23	1.29	1.32	1.31	1.25	1.10
0.25	0.74	0.90	1.02	1.10	1.14	1.17	1.15	1.09	0.94
0	0.64	0.78	0.89	0.96	1.00	1.01	1.00	0.93	0.79
−0.25	0.53	0.66	0.76	0.83	0.86	0.86	0.84	0.77	0.64
−0.5	0.43	0.55	0.63	0.69	0.71	0.71	0.68	0.61	0.49
−0.75	0.34	0.44	0.51	0.56	0.57	0.56	0.52	0.44	0.34
−1	0.27	0.36	0.41	0.43	0.43	0.41	0.37	0.30	0.24
(**b**) $F/(1+F) = 0.4$									
1	1.05	1.20	1.31	1.38	1.44	1.49	1.53	1.56	1.49
0.75	0.95	1.10	1.20	1.27	1.33	1.38	1.41	1.43	1.35
0.5	0.86	1.00	1.10	1.17	1.22	1.26	1.29	1.29	1.20
0.25	0.77	0.91	1.00	1.06	1.11	1.15	1.17	1.16	1.05
0	0.68	0.81	0.90	0.96	1.00	1.03	1.05	1.03	0.90
−0.25	0.59	0.72	0.80	0.85	0.89	0.92	0.93	0.90	0.75
−0.5	0.52	0.63	0.71	0.75	0.79	0.81	0.81	0.77	0.61
−0.75	0.45	0.56	0.62	0.66	0.68	0.70	0.69	0.64	0.46
−1	0.42	0.50	0.55	0.57	0.58	0.59	0.57	0.52	0.39
(**c**) $F/(1+F) = 0.5$									
1	1.05	1.16	1.23	1.28	1.32	1.36	1.41	1.46	1.50
0.75	0.97	1.08	1.15	1.20	1.24	1.28	1.32	1.37	1.40
0.5	0.89	1.00	1.07	1.12	1.16	1.20	1.23	1.27	1.30
0.25	0.82	0.93	0.99	1.04	1.08	1.11	1.15	1.18	1.20
0	0.75	0.86	0.92	0.96	1.00	1.03	1.06	1.09	1.10
−0.25	0.70	0.80	0.85	0.89	0.93	0.95	0.98	1.00	0.99
−0.5	0.65	0.74	0.79	0.83	0.85	0.88	0.90	0.92	0.89
−0.75	0.62	0.70	0.74	0.77	0.79	0.81	0.82	0.83	0.79
−1	0.60	0.67	0.70	0.71	0.73	0.74	0.74	0.74	0.69
(**d**) $F/(1+F) = 0.6$									
1	1.07	1.15	1.19	1.23	1.26	1.29	1.32	1.36	1.43
0.75	1.00	1.08	1.12	1.16	1.19	1.22	1.25	1.29	1.35
0.5	0.94	1.02	1.06	1.09	1.12	1.15	1.18	1.22	1.28
0.25	0.89	0.96	1.00	1.03	1.06	1.09	1.11	1.15	1.21
0	0.84	0.91	0.95	0.98	1.00	1.02	1.05	1.08	1.13
−0.25	0.81	0.87	0.90	0.92	0.95	0.97	0.99	1.02	1.06
−0.5	0.78	0.83	0.86	0.88	0.90	0.91	0.93	0.96	0.99
−0.75	0.76	0.80	0.83	0.84	0.86	0.87	0.88	0.90	0.92
−1	0.75	0.78	0.80	0.81	0.82	0.83	0.84	0.84	0.85
(**e**) $F/(1+F) = 0.7$									
1	1.11	1.16	1.19	1.22	1.24	1.26	1.28	1.31	1.37
0.75	1.04	1.10	1.13	1.15	1.17	1.19	1.21	1.25	1.30

Table 1 continued

$\varphi\downarrow\quad\delta\rightarrow$	60°	45°	30°	15°	0°	−15°	−30°	−45°	−60°
0.5	0.99	1.04	1.07	1.09	1.11	1.13	1.15	1.18	1.23
0.25	0.94	0.98	1.01	1.03	1.05	1.07	1.09	1.12	1.17
0	0.90	0.94	0.97	0.98	1.00	1.02	1.04	1.06	1.10
−0.25	0.87	0.90	0.93	0.94	0.95	0.97	0.98	1.01	1.04
−0.5	0.85	0.87	0.89	0.91	0.92	0.93	0.94	0.96	0.99
−0.75	0.83	0.85	0.87	0.88	0.88	0.89	0.90	0.92	0.94
−1	0.82	0.84	0.85	0.85	0.86	0.86	0.87	0.88	0.89
(**f**) $F/(1+F)=0.8$									
1	1.16	1.20	1.22	1.23	1.25	1.26	1.27	1.29	1.33
0.75	1.09	1.13	1.15	1.16	1.18	1.19	1.20	1.23	1.26
0.5	1.03	1.07	1.09	1.10	1.11	1.12	1.14	1.16	1.19
0.25	0.98	1.01	1.03	1.04	1.05	1.06	1.08	1.10	1.13
0	0.94	0.96	0.98	0.99	1.00	1.01	1.02	1.04	1.07
−0.25	0.90	0.92	0.94	0.95	0.95	0.96	0.97	0.99	1.01
−0.5	0.87	0.89	0.90	0.91	0.92	0.92	0.93	0.94	0.96
−0.75	0.85	0.87	0.88	0.88	0.89	0.89	0.90	0.91	0.92
−1	0.84	0.85	0.86	0.86	0.86	0.87	0.87	0.88	0.89

$$4\pi G \approx \frac{-1}{r}+\frac{1}{r_1}-\frac{2}{F^2+r_1}-\frac{2F^2\psi}{(F^2+r_1)^2}\left(1+\frac{2.3\,\psi\, r_1}{F^2+r_1}\right) + H(x-\widetilde{x})\frac{8}{F^2}\,\Im\mathfrak{m}\int_0^\infty \mathrm{d}t\; \mathrm{e}^{(1+t^2)(z+\widetilde{z})/F^2-\mathrm{i}\sqrt{1+t^2}(x-\widetilde{x})/F^2} \tag{50a}$$

with

$$\left.\begin{aligned} r &= \sqrt{(x-\widetilde{x})^2+(z-\widetilde{z})^2}\\ r_1 &= \sqrt{(x-\widetilde{x})^2+(z+\widetilde{z})^2}\end{aligned}\right\}\quad \psi=\frac{-(z+\widetilde{z})}{r_1+|x-\widetilde{x}|}\quad F=\frac{V_s}{\sqrt{gL_{\mathrm{ref}}}}, \tag{50b}$$

as readily follows from (25), (23) and (12). The Green function (50) of thin-ship theory is considerably simpler than the Green functions given in the literature, e.g. [11, 12, 17, 18]. In particular, the double integral that defines the local flow component in the well-known representations given in the literature, e.g. [7–9, 11, 18], has been approximated by a simple analytical expression, valid within the entire flow domain $0\le r_1\le\infty$, in (50). Although the local-flow component in the approximate Green function (50) is not highly accurate, as shown in Fig. 13, the calculations reported in the study show that the approximation (50) is sufficient. This result stems from two main properties: (i) the contribution of the wave component in (50a) typically is more important than that of the local-flow component, and (ii) the approximate local-flow component in (50a) is asymptotically correct in both the nearfield and the farfield. An analogous Green function for evaluating steady flow due to a distribution of pressure at the free surface, for which we have $z+\widetilde{z}=0$, is reported in [22]. The general case $y-\widetilde{y}\neq 0$ and $z+\widetilde{z}\neq 0$ will also be reported elsewhere.

Another practical result is the simple relations

$$\frac{Z_b\,g}{V_s^2}\approx(\tan\alpha+\tan\alpha')\,\frac{1.1}{1+F}\,\zeta_b(F,\delta,\varphi),\qquad \frac{-X_b\,g}{V_s^2}\approx\frac{1.1}{1+F}\,\xi_b(F,\delta,\varphi) \tag{51a}$$

with

$$F\equiv\frac{V_s}{\sqrt{gD}}\quad\text{and}\quad\varphi\equiv\frac{\tan\alpha-\tan\alpha'}{\tan\alpha+\tan\alpha'} \tag{51b}$$

Table 2 Function $\xi_b(F, \delta, \varphi)$ defined by (48c) for (**a**) $F/(1+F) = 0.3$, (**b**) $F/(1+F) = 0.4$, (**c**) $F/(1+F) = 0.5$, (**d**) $F/(1+F) = 0.6$, (**e**) $F/(1+F) = 0.7$, and (**f**) $F/(1+F) = 0.8$

$\varphi \downarrow \quad \delta \rightarrow$	60°	45°	30°	15°	0°	−15°	−30°	−45°	−60°
(**a**) $F/(1+F) = 0.3$									
1	1.83	1.57	1.35	1.15	0.97	0.80	0.62	0.45	0.28
0.75	1.85	1.59	1.37	1.16	0.97	0.80	0.62	0.45	0.28
0.5	1.88	1.62	1.39	1.18	0.98	0.80	0.62	0.44	0.28
0.25	1.92	1.66	1.43	1.20	0.99	0.80	0.62	0.43	0.27
0	1.98	1.71	1.47	1.23	1.00	0.80	0.60	0.42	0.27
−0.25	2.08	1.81	1.54	1.27	1.02	0.80	0.59	0.41	0.26
−0.5	2.28	1.97	1.67	1.34	1.04	0.80	0.57	0.39	0.25
−0.75	2.74	2.32	1.91	1.47	1.10	0.80	0.53	0.33	0.21
−1	4.12	3.15	2.43	1.74	1.25	0.81	0.36	−0.96	−5.50
(**b**) $F/(1+F) = 0.4$									
1	1.62	1.37	1.19	1.03	0.90	0.77	0.63	0.47	0.30
0.75	1.66	1.41	1.21	1.06	0.91	0.78	0.63	0.47	0.30
0.5	1.71	1.45	1.26	1.09	0.94	0.79	0.63	0.47	0.29
0.25	1.79	1.53	1.31	1.13	0.96	0.80	0.64	0.45	0.28
0	1.91	1.62	1.39	1.18	1.00	0.82	0.64	0.45	0.26
−0.25	2.08	1.76	1.49	1.25	1.05	0.85	0.64	0.43	0.24
−0.5	2.36	1.97	1.62	1.35	1.11	0.88	0.64	0.41	0.21
−0.75	2.83	2.26	1.82	1.50	1.21	0.94	0.66	0.37	0.15
−1	3.45	2.62	2.08	1.69	1.35	1.02	0.67	0.25	−1.27
(**c**) $F/(1+F) = 0.5$									
1	1.41	1.18	1.03	0.91	0.82	0.73	0.63	0.52	0.36
0.75	1.48	1.24	1.08	0.96	0.85	0.75	0.65	0.52	0.36
0.50	1.57	1.31	1.14	1.01	0.89	0.78	0.67	0.53	0.35
0.25	1.70	1.41	1.21	1.07	0.94	0.82	0.69	0.54	0.35
0	1.87	1.53	1.31	1.14	1.00	0.87	0.72	0.55	0.34
−0.25	2.09	1.68	1.43	1.23	1.08	0.92	0.76	0.57	0.33
−0.50	2.33	1.85	1.55	1.34	1.16	0.99	0.81	0.59	0.32
−0.75	2.58	2.02	1.70	1.46	1.26	1.07	0.87	0.62	0.29
−1	2.81	2.19	1.84	1.59	1.38	1.17	0.95	0.66	0.24
(**d**) $F/(1+F) = 0.6$									
1	1.20	1.01	0.90	0.82	0.75	0.69	0.63	0.55	0.42
0.75	1.29	1.08	0.95	0.87	0.80	0.73	0.66	0.57	0.43
0.50	1.41	1.17	1.03	0.93	0.85	0.78	0.69	0.59	0.44
0.25	1.55	1.28	1.13	1.01	0.92	0.83	0.74	0.62	0.46
0	1.72	1.40	1.23	1.11	1.00	0.90	0.79	0.66	0.48
−0.25	1.88	1.54	1.34	1.21	1.10	0.98	0.86	0.71	0.50
−0.5	2.04	1.67	1.46	1.32	1.19	1.07	0.94	0.78	0.53
−0.75	2.18	1.79	1.58	1.42	1.29	1.17	1.03	0.85	0.58
−1	2.30	1.90	1.68	1.53	1.39	1.27	1.12	0.93	0.64
(**e**) $F/(1+F) = 0.7$									
1	1.01	0.88	0.81	0.76	0.72	0.68	0.63	0.58	0.49

Table 2 continued

$\varphi \downarrow \quad \delta \rightarrow$	60°	45°	30°	15°	0°	−15°	−30°	−45°	−60°
0.75	1.10	0.95	0.87	0.81	0.76	0.72	0.67	0.61	0.51
0.5	1.22	1.04	0.94	0.88	0.83	0.78	0.72	0.65	0.54
0.25	1.35	1.15	1.04	0.97	0.90	0.85	0.79	0.70	0.57
0	1.50	1.28	1.16	1.07	1.00	0.93	0.86	0.76	0.62
−0.25	1.64	1.41	1.28	1.19	1.11	1.03	0.95	0.85	0.68
−0.5	1.78	1.54	1.40	1.30	1.22	1.14	1.05	0.94	0.75
−0.75	1.90	1.65	1.51	1.41	1.33	1.25	1.16	1.03	0.84
−1	2.00	1.75	1.62	1.52	1.43	1.35	1.26	1.13	0.93
(**f**) $F/(1+F) = 0.8$									
1	0.87	0.80	0.75	0.72	0.70	0.68	0.65	0.62	0.56
0.75	0.94	0.86	0.81	0.78	0.75	0.73	0.70	0.66	0.59
0.5	1.04	0.94	0.89	0.85	0.82	0.78	0.75	0.70	0.63
0.25	1.15	1.04	0.98	0.94	0.90	0.86	0.82	0.77	0.69
0	1.29	1.16	1.09	1.04	1.00	0.96	0.91	0.85	0.76
−0.25	1.43	1.29	1.21	1.16	1.11	1.07	1.02	0.95	0.84
−0.5	1.56	1.42	1.34	1.28	1.23	1.18	1.13	1.06	0.94
−0.75	1.68	1.54	1.46	1.40	1.35	1.30	1.25	1.17	1.04
−1	1.79	1.65	1.57	1.51	1.46	1.41	1.35	1.28	1.15

for the height Z_b and the location $-X_b$ of the bow wave generated by a ship bow with rake and flare, as shown in Figs. 1 and 24. These relations account for the influence of the rake angle δ and the flare parameter φ on the bow-wave height Z_b and location $-X_b$ via the functions $\zeta_b(F, \delta, \varphi)$ and $\xi_b(F, \delta, \varphi)$. These two functions—determined using thin-ship theory—provide corrections to the relations given in [1, 2] for the special case of wedge-ended ship bows without rake and flare, for which we have $\zeta_b = 1$ and $\xi_b = 1$ in (51a). The simple analytical relations (51) and the twelve Tables 1a–f and 2a–f of values of the functions ζ_b and ξ_b provide estimates of the bow-wave height Z_b and location $-X_b$ for a broad class of ship bows with rake and flare. These tables and (51) can be used immediately—without hydrodynamic calculations—for ship design. The results depicted in Figs. 25–27 and listed in Tables 1a–f and 2a–f show that rake and flare can have large effects, especially at low Froude numbers.

Expressions (51a) with $\zeta_b = 1$ and $\xi_b = 1$, i.e., for the special case $\delta = 0$ and $\varphi = 0$, are shown in [1, 2] to be in reasonable agreement with experimental measurements for both wedge-shaped ship bows and a rectangular flat plate. The comparisons between experimental measurements and theoretical predictions reported in Fig. 16 for the Wigley hull and in Figs. 21–23 (and the Table related to Fig. 23) for wedge-shaped ship bows show that the use of thin-ship theory, adopted here, to extend the relations given in [1, 2] to the more general case $\delta \neq 0$ and $\varphi \neq 0$ is appropriate for fine ship bows (i.e. for a large class of fast ships). Thus, the approach followed in [1, 2] and here to obtain (51a) is experimentally validated, at least to some extent, by the comparisons between experimental measurements and theoretical predictions reported in Figs. 16, 21–23 and in [1, 2]. These comparisons also provide an indication of the accuracy that can reasonably be expected from the simple relations (51a). Additional comparisons, for a large set of ship bows with rake and flare, would of course be useful.

The Bernoulli bound $Z\, g/V_s^2 \leq 1/2$ for steady free-surface flows considered in [1] shows that ship bow waves are necessarily unsteady if $1/2 < Z_b\, g/V_s^2$, i.e., if

$$F \leq 2.2(\tan\alpha + \tan\alpha')\zeta_b(F, \delta, \varphi) - 1. \tag{52}$$

Thus, (51a) is not valid in the unsteady-bow-wave regime defined by (52), i.e. for relatively large average waterline entrance angle $\alpha + \alpha'$. Indeed, [1] shows that we have $Z_b\, g/V_s^2 \approx 1/2$ in the unsteady regime (52).

A four-parameter family of simple ruled ship bows has been considered here for two main reasons: (i) the four parameters $\alpha + \alpha'$, δ, φ and F are major parameters that have a dominant influence on a ship bow wave, and (ii) the limited number of parameters involved in this family of ship bows made it possible to perform a systematic parametric study and to obtain results—specifically, the functions $\zeta_b(F, \delta, \varphi)$ and $\xi_b(F, \delta, \varphi)$ listed in Tables 1a–f and 2a–f—that can be used immediately, without hydrodynamic calculations. A more general family of ship bows that accounts for the hull curvature would involve a significantly greater number of parameters, for which a systematic parametric study would be problematic. However, the highly-simplified thin-ship theory given here provides a practical basis for considering more complex ship bows.

Acknowledgements This work was sponsored by the Naval Surface Warfare Center Carderock Division (NSWCCD) in support of the Naval Sea Systems Command's Joint High Speed Sealift (JHSS) Program (Technical Monitors: Mr. Robert Anderson and Mr. John Offutt, JHSS Technology Managers) and by the Office of Naval Research (Technical Monitor: Ms. Kelly Cooper) and the ILIR Program at NSWCCD (Technical Monitor: Dr. John Barkyoumb).

References

1. Noblesse F, Delhommeau G, Guilbaud M, Hendrix D, Yang C (2008) Simple analytical relations for ship bow waves. J Fluid Mech 600:105–132
2. Noblesse F, Hendrix D, Faul L, Slutsky J (2006) Simple analytical expressions for the height, location, and steepness of a ship bow wave. J Ship Res 50:360–370
3. Noblesse F, Delhommeau G, Guilbaud M, Yang C (2008) The rise of water at a ship stem. J Ship Res 52:89–101
4. Faltinsen OM (2005) Hydrodynamics of high-speed marine vehicles. Cambridge University Press, Cambridge, 454 pp
5. Day AH, Doctors LJ (2001) Rapid evaluation of near and far field wave wake from ships and application to hull form design and optimization. J Ship Res 45:73–84
6. Stoker JJ (1957) Water waves. Interscience, New York
7. Kostyukov AA (1959) Theory of ship waves and wave resistance. English translation 1968, ECI, Iowa City, Sudpromfiz, Leningrad
8. Wehausen JV, Laitone EV (1960) Surface waves. In: Encyclopedia of Physics, vol 9. Springer-Verlag, Berlin
9. Wehausen JV (1973) The wave resistance of ships. Adv Appli Mech 13:93–245
10. Standing RG (1974) Phase and amplitude discrepancies in the surface wave due to a wedge-ended hull form. J Fluid Mech 62:625–642
11. Noblesse F (1981) Alternative integral representations for the Green function of the theory of ship wave resistance. J Eng Math 15:241–265
12. Ponizy B, Noblesse F, Ba M, Guilbaud M (1994) Numerical evaluation of free-surface Green functions. J Ship Res 38:193–202
13. Noblesse F (1978) On the fundamental function in the theory of steady motion of ships. J Ship Res 22:212–215
14. Noblesse F (1975) The near-field disturbance in the centerplane Havelock source potential. In: 1st IL conference on numerical ship hydrodynamics, Washington, DC, pp 481–501
15. Telste JG, Noblesse F (1989) The nonoscillatory near-field term in the Green function for steady flow about a ship. In: 17th symposium on naval hydrodynamics, The Hague, pp 39–52
16. Noblesse F (1978) The steady wave potential of a unit source, at the centerplane. J Ship Res 22:80–88
17. Masson E, DeBayser O, Martin D (1991) Evaluation de la resistance de vagues d'un sous-marin en immersion totale. 3emes Journèes de l'Hydro, Grenoble, France
18. Newman JN (1987) Evaluation of the wave resistance Green function: part 1—the double integral. J Ship Res 31:79–90
19. Lyness JN, Jespersen D (1975) Moderate degree symmetric quadrature rules for the triangle. J Inst Math Appl 15:19–32
20. McCarthy JH (1985) Collected experimental resistance and flow data for three surface ship model hulls. David W Taylor Naval Ship Research and Development Center, report DTNSRDC-85/011
21. Cooperative experiments on Wigley parabolic model in Japan. In: 17th ITTC resistance committee report
22. Noblesse F, Delhommeau G, Yang C (2008) Practical evaluation of steady flow due to a free-surface pressure patch. J Ship Res (submitted)